Investigation into the impact of solid surfaces in aqueous systems

Bjørnar Jensen

Dissertation for the degree of philosophiae doctor (PhD)
at the University of Bergen

2016

Dissertation date: 3.3.2016

To my wife and family.
My pillars of support.

Scientific environment

The research in this PhD thesis have been performed at the University of Bergen, Institute of Physics and Technology in the group for thermodynamic modeling. My main supervisors have been Professor Bjørn Kvamme and Professor Tatiana Kuznetsova have been my co-supervisor.

The work presented herein have been part of larger research projects and funded by FME-SUCCESS with additional funding from Statoil ASA.

Acknowledgements

Is has been a long journey. From the start, and finally, to the finish of this journey – this thesis – I have had moments of despair, moments of complacency, moments of adversity and moments of success.

On the path ventured surprises have been unveiled. Life is different now. Better. My wife, Cornelia, whom I met on this path has supported me and endured with me. For this I am truly thankful. My family, parents and sister, have also always been there for me. Supported me, believed in me and cheered for me. I am fortunate to have you and for being allowed to thank you. Thank you!

The work I have done – what I have accomplished – would never have been accomplished if not for my supervisors. Professor Bjørn Kvamme and Professor Tatiana Kuznetsova. Prof. Kvamme took early a personal interest in my work during my master thesis. He encouraged me to apply for a Ph.D. position. As said as done. Here we are, a bit later than planned, but at the end of a Ph.D. Thank you for you interest. For the encouragement, the discussions, the meetings and travels. Your grand ideas, your visions, they are an inspiration.

Prof. Kuznetsova were always on hand for fruitful discussions both in regards to the work and other less serious topics. I can even recall her working, solely for my benefit, during a weekend or two. You are never one to say no when a candidate of yours are in need of help. The door to your office is always open, and I have always been welcome. Thank you. Hours of discussion, hours of troubleshooting, hours of writing. You never give up, always prevail and are always helpful.

My colleagues and fellow Ph.D. candidates. There are so many of you, and I owe you all a big "thank you". Some I have had the pleasure to get to know really good. Some I have shared office with, on masters or during Ph.D. During my stay Khuram Baig has been here, from masters to Ph.D. We have walked the same path, and had many interesting sessions. To those that have gone before me, Ashok Chejara, Muhammad Qasim, Shunping Liu, Phan Van Cuong, Khaled Jemai and Mohammad Taghi Vafaei. Thank you all for discussions in the office, conversations in the hallway and in general the welcome atmosphere you all contributed to.

Sara J. Sjöblom, thank you for being yourself. I have enjoyed tremendously the conversations, in particular the conversations on literature. Great authors, books to read, and soon your own contribution to the area. While perhaps not the most productive of days, I have fond memories of the days where I walked into my office, finding you in conversation with Richard, dressed in your colorful outfits. Those days were always good, even though they were unproductive.

I thank you Richard Olsen, for sharing the office, for participating in discussions, for guidance in regards to C++ best-practices. I have clearly had a benefit of sharing my office with you. We have had lengthy discussions, long sessions troubleshooting

and debugging. We have agreed and disagreed, collaborated and worked independently. In the end I believe we both may have become better scientists as a result. Khadijeh Qorbani and Kim Nes Leirvik, while on different floors we have had many occasions to talk, discuss and have fun. Kadijeh is always polite, positive and welcome with a smile. I wish you the best of success. Thank you for all the good times. Kim, from master degree to Ph.D. you have an athlete's mentality. Positive, problem solver with an curious intellect. Always chasing the solution not just satisfied with asking the question. The cup of tea, never leaving your side. You have a strong ability to think for yourself, work the problems and finding the solutions. And always happy. Always. Thank you, it is a pleasure knowing you!

The rest, those I forgot or neglected to mention; your name should probably be right about here. In the list of all those names, all those friends, colleagues, acquaintances and family members, the ones that have supported me, helped me and distracted me when necessary ...

Thank you all!

Abstract

Global warming is upon us. The scientific community is searching for methods of slowing down, preventing and reversing its effects. Carbon dioxide have been at the center of attention the last few decades, being the main contributor to man-made global warming. Carbon capture and sequestration is one of the potential tools in this undertaking of mitigation. By capturing carbon dioxide and transporting it to injection sites for subsurface storage the amount released can be reduced.

This thesis approaches several of the topics involved in transport and sequestration of carbon dioxide. Carbon dioxide transport to injection site will likely be by pipelines. In arctic regions the potential for ice-like structures known as clathrates, or hydrates, to form due to the high pressure and low temperature conditions is significant. Reducing the risks of hydrate formation calls for knowledge of the decisive factors. Thus, this work participates in the development of more robust strategies for hydrate prediction and consequently prevention.

In pipelines, oxidized carbon steel surfaces are readily available. These have proven to be excellent adsorption sites for water in the gas stream. Carbon dioxide is an hydrate former, capable of stabilizing hydrate cavities of water molecules as a guest molecule. Here the chemical potential of water, carbon dioxide and hydrogen sulfide is examined under realistic pipeline conditions. These results are used to predict if, in which phase, and from which phases, hydrate will form. It was found that water will adsorb onto the hematite (rust) surface. The water layers closest to the hematite have too low chemical potential for hydrates to form. However, as the distance to the hematite increases, water regains more and more of its bulk properties, where hydrates are possible. Adsorbed impurities like hydrogen sulfide is shown to assist carbon dioxide in forming stable hydrates. We draw the conclusion that relying solely on dew-point calculations may underestimate the risk of hydrate formation.

Reducing the risk of hydrate formation can also be done by gas dehydration. As the hydrate cavities consists of hydrogen bonded water molecules, reducing available water will serve as a method of hydrate prevention. Linde Type A zeolites is often used in processing industry for gas dehydration. However, detailed information on kinetics such as rate of loading, diffusion and poisoning can still be improved. This work investigates the interfacial termination of Linde Type A zeolites. Furthermore, the effects of partial atomic charges in the interface region on diffusion, flux and water orientation and structuring are determined.

It was found that while the termination mattered, the charge distribution dominated and significantly affected the kinetics in the interface region. Likewise, improper balancing of partial atomic charges led to disturbances in the inter-cavity motion of water molecules. Depending on the distribution of charges in the interface the rate of loading were reduced by as much as half.

List of publications

Papers

I P. V. Cuong, B. Kvamme, T. Kuznetsova, and B. Jensen. “Molecular dynamics study of calcite, hydrate and the temperature effect on CO2 transport and adsorption stability in geological formations”. *Molecular Physics* **110**, 11-12, pp. 1097–1106, (2012)

II B. Kvamme, T. Kuznetsova, B. Jensen, S. Stensholt, J. Bauman, S. Sjöblom, and K. Nes Lervik. “Consequences of CO2 solubility for hydrate formation from carbon dioxide containing water and other impurities”. *Physical Chemistry Chemical Physics.* **16**, 18, pp. 8623–8638, (2014)

III T. Kuznetsova, B. Jensen, B. Kvamme, and S. Sjöblom. “Water-wetting surfaces as hydrate promoters during transport of carbon dioxide with impurities”.*Physical Chemistry Chemical Physics* **17**, 19, pp. 12683–12697, (2015).

IV B. Jensen, T. Kuznetsova, B. Kvamme, and R. Olsen. “The impact of electrostatics in bulk Linde Type A zeolites”. *Microporous and Mesoporous Materials* **201**, 0, pp. 105-115, (2015)

V B. Jensen, B. Kvamme, and T. Kuznetsova. “The effect of interfacial charge distributions and terminations in LTA zeolites”. *Microporous and Mesoporous Materials* N/A. Status: Accepted manuscript, N/A. (2015)

International presentations

I B. Jensen, B. Kvamme, T. Kuznetsova, K. O. Christensen, A. C. M. Miguens, and E. Solbraa. “Evaluation of Zeolite LTA-Force Fields for Molecular Dynamics Simulation Purposes”. *Molecular Simulation 7 - Forcefields.* Presented by Bjørn Kvamme. Eighteenth Symposium on Thermophysical Properties. June 2012.

II B. Jensen, T. Kuznetsova, B. Kvamme, E. Solbraa, and A. C. M. Miguens. “Molecular Dynamics Investigation of Triethylene Glycol in hydrated LTA Zeolite - Emphasis on Evaluation of Potential Models.” *Industrial use of Molecular Thermodynamics.* Presented by Bjørnar Jensen. InMoTher 2012. Mar. 2012.

III B. Jensen, T. Kuznetsova, B. Kvamme, A. C. M. Miguens, K. O. Christensen, and E. Solbraa. “Triethylene Glycol - Adsorption and Interaction with LTA Zeolite”. *Molecular Simulation 5 - Confined Fluids.* Presented by Bjørnar Jensen. Eighteenth Symposium on Thermophysical Properties. June 2012.

Contents

List of Figures

Abbreviations

AR4	fourth assessment report
AR5	fifth assessment report
CCS	carbon capture and sequestration
CPU	central processing unit
EOR	enhanced oil recovery
fSPC	flexible simple point charge
GHG	greenhouse gas
GMST	global mean surface temperature
GPGPU	general purpose graphical processing unit
HSE	health, safety and the environment
IPCC	Intergovernmental Panel on Climate Change
LTA	Linde type A
LTA-3A	Linde type A zeolites with potassium counter-ions
LTA-4A	Linde type A zeolites with sodium counter-ions
MD	molecular dynamics
MOF	metal organic framework
MSD	mean squared displacement
PBC	periodic boundary conditions
ppb	parts per billion
ppmV	parts per million by volume
RF	radiative forcing
SPC	simple point charge
SPC/E	extended simple point charge

syngas	synthesis gas
Tcl	tool command language
vdW	van der Waals
VMD	Visual Molecular Dynamics
WMGHG	well-mixed greenhouse gas

Chemicals

Ca^{2+}	calcium ion
$CaCO_3$	calcite
CH_4	methane
$\left\|M^{n+}_{12/n}\right\|_8[Al_{12}Si_{12}O_{48}]_8$	LTA (generic formula)
CO	carbon monoxide
CO_2	carbon dioxide
CO_3^{2-}	carbonate ion
Fe^{2+}	ferrous ion
$FeCO_3$	siderite
H_2	hydrogen gas
H_2O	water
H_2S	hydrogen sulfide
Fe_2O_3	hematite
$MgCO_3$	magnesite
N_2O	nitrous oxide
TEG	tri-ethylene glycol

Symbols

α	Morse potential well width
β	Ewald coefficient
δ_{ij}	scaling factor for interaction between i and j
ε_0	permittivity of vacuum
ε	Lennard-Jones well depth or strength of interaction
ε_{ij}	ε for interaction between atoms i and j
ε_r	relative permittivity
ϕ	dihedral angle
σ	Lennard-Jones parameter
σ_{ij}	σ for interaction between atoms i and j
θ	angle between bonded atoms A–B–C
θ_{eq}	equilibrium angle between bonded atoms A–B–C
ζ	Nosé-Hoover thermodynamic friction coefficient
$\langle A \rangle$	ensemble average of property A
A	Buckingham potential exponential pre-factor (repulsive)
$\mathcal{A}$	System in state $\mathcal{A}$
$A(t)$	value of property A as function of time, t
$\overline{A(t)}$	time-average of property $A(t)$
B	Buckingham potential parameter (in exponential function)
$\mathcal{B}$	System in state $\mathcal{B}$
C	Buckingham potential parameter (attractive)
D_e	Morse potential well depth
E	energy
$\mathbf{F}$	force
i	particle iterator
j	particle iterator

k_b	force constant for a bond
k_f	force constant for an angle
N	number of particles
p	pressure
$\mathbf{p}$	momentum
p_s	time-scale conjugated momentum
Q	Nosé-Hoover thermostat parameter
$\mathbf{q}$	position
q_c	partial atomic charge of particle
Q_i	partial atomic charge of particle i
Q_j	partial atomic charge of particle j
r	bond or separation length
$R\bar{3}c$	a trigonal crystallographic space group
r_{eq}	equilibrium bond length
$\mathbf{r}$	vector between two particles
s	time-scale variable
T	temperature
t	time
U	potential energy
U_{angle}	potential energy from angle bending
U_{bond}	potential energy from bond stretching
$U_{dihedral}$	potential energy from twisting a dihedral angle
U_{el}	potential energy from electrostatic interactions
U_{vdW}	potential energy from van der Waals interactions
V	volume
$V_1 \ldots V_3$	dihedral force constants
X	number of independent degrees of freedom in $\mathbf{q}$ and $\mathbf{p}$

Chapter 1: Introduction

CO_2 have been at the center of attention the last few decades, being the main contributor to man-made global warming. In 1997 the Kyoto Protocol [1] was adopted. In the Kyoto Protocol the parties agreed to reduce the carbon dioxide equivalent emissions by at least 5% from the 1990-level, in the period 2008-2012.

To reduce the carbon dioxide emissions renewable energy sources must be utilized while weakening fossil fuel dependence. Reduction of CO_2 emissions by post-combustion capture is also viable. Large stationary carbon dioxide sources, like coal power plants, are good candidates for carbon capture and sequestration (CCS). By scrubbing the flue-gas for carbon dioxide, the CO_2 can be captured and stored in geological formations. While technology for capturing carbon dioxide (i.e. natural gas treatment with amines) was first disclosed in 1959 by Bertheir [2], subsurface storage is in need of some attention from the research community.

When injecting carbon dioxide in geological formations, proper sealing of the reservoir is key. The site has to be thoroughly examined to identify faults in the cap-rock, designating regions that potentially should be avoided. To further add to a complex picture, carbon dioxide can dissolve into water and lower the pH. For subterranean sequestration of CO_2 where depleted hydrocarbon reservoirs are among the more obvious choices, the mineral composition of the reservoir rock is important. One of the more abundant minerals in earths crust, calcite ($CaCO_3$), can be dissolved by aqueous carbon dioxide. This give rise to the possibility of fractures being widened, permeabilities that may change due to dissolution or precipitation, or eventually leakage.

For off-shore subsurface storage carbon dioxide has to be transported to the injection site. While pipelines likely is the best option for such transport, it is not without problematic issues. Pipeline transport of CO_2 may be complicated by the presence of trace amounts of water. If the pipeline happens to be located on the sea-floor, or in arctic areas, the low temperatures combined with the high pressures inside may cause clathrates to form. Formation of hydrates (clathrates) can lead to blocking of the pipeline, with the consequences that may have.

Gas hydrate consists of water forming the cavities and guest molecules filling the cavities and stabilizing the hydrates. Without water, guest molecules or correct pressure and temperature conditions, hydrates cannot form. There exists several strategies for preventing hydrate formation. One could be to operate with pressure and temperature conditions that will not allow for hydrates to form. Another would be to inject chemicals, like methanol or ethylene glycol, diethylene glycol or triethylene glycol. These prevent hydrate formation by favorable hydrogen bonding to water, lowering the chemical potential of the aqueous phase. However, just like hydrate inhibitors may prevent hydrate formation, surfaces and interfaces may contribute to promote hydrate formation.

In daily life interfaces play a crucial role in an abundance of processes, from biological to chemical and further to physical processes. Interfaces, like cell-membranes, are vital for life as we know it. Interfaces are also present in industrial systems. For instance in oil-water gravitational separators, distillation columns, packed column absorption systems and even in pipelines. In short, all systems containing more than one phase has to have at least one interface.

While a pipeline wall macroscopically might seem like a uniform surface, microscopically it is quite complex. The surface might have been exposed to water, or humidity, and as a consequence rusted. Or, it might have been coated with an surface active agent. Between the rusty spots, or surface, there might be small gaps or wide bands of unoxidized iron. On a molecular scale, all these surfaces have different properties, resulting in disparate interactions between the surface and neighboring molecules. For instance, the rusty surface will be highly hydrophilic, while the surfactant coated surface can be hydrophobic. The differences in interactions between water and seemingly similar surfaces is controlled at the atomistic/molecular, or even quantum, level. Understanding hydrate formation, and proper prevention, requires knowledge of how surfaces affect hydrate constituents, stability and structure.

As water has to be present for hydrates to form, simply drying the gas and removing water from the fluid is a viable option. Gas drying can be achieved in different manners. One of the methods involves using zeolites to adsorb the water. The benefit of this method is that it can be tuned to selectively adsorb water, while ignoring for instance carbon dioxide.

A zeolite often used for drying of natural gas is the Linde type A (LTA) zeolite. LTA zeolites is a cubic structure with cavities inside. By ion-exchange different counter-ions can be introduced into the zeolite, effectively blocking part of the entrances. Consequently, the zeolite works as a molecular sieve, only allowing molecules with physical dimensions below certain sizes access to the interior. For instance, Linde type A zeolites with sodium counter-ions (LTA-4A) will allow both water and methane access, where Linde type A zeolites with potassium counter-ions (LTA-3A) will only allow water of the two.

While LTA zeolites have received considerable attention the last decade or so, questions still remains when it comes to its kinetic properties. In particularly there has been a lack of attention on how the interface is terminated, the effect of the termination, and how the interface facilitates or prevent poisoning of the zeolite.

1.1 Objectives and outline of thesis

The focus of this thesis is within the realm of CCS to examine the potential for hydrate formation when CO_2 is subjected to pipeline transport, subterranean injection and storage. Furthermore, to investigate LTA zeolites, to eventually optimize the loading and reduce potential poisoning of the zeolites.

From the main objective the following sub-objectives have been derived:

- Determine the structure and chemical potential of water on calcite surface
- Determine the structure and chemical potential of water on hematite

- Evaluate the potential for hydrate formation on said surfaces
- Investigate the impact of LTA zeolite termination on water interaction and adsorption

With this in mind the following systems are studied in this thesis:

I Calcite with water and carbon dioxide

II Hematite with water and carbon dioxide

III Hematite with water and hydrogen sulfide

IV Linde Type A zeolites with water (both potassium and sodium counter-ions)

The rather wide scope of the main objective does imply that this is part of a larger work. Thus, the focus in this thesis is mainly on the zeolite and effect of termination and charges in those systems. However, the first papers were on systems with calcite and hematite where I contributed by writing analysis routines, extending software and implementing free energy calculation methods, and running simulations with subsequent post-processing. It ends with the two papers on LTA zeolites, where the focus is on the water-zeolite interactions, the electrostatic interactions and the effect of termination and charge distributions in the interface.

The whole thesis could easily have been dedicated to just one of the sub-goals. Nevertheless, it has to fit into a larger scope.

Chapter 2: Background

2.1 Global warming

According to overwhelming international consensus, and backed up by the massive reports from the Intergovernmental Panel on Climate Change (IPCC), climate change is happening right now, and the humankind is to blame. IPCC's fifth assessment report (AR5) states that it is certain that the global mean surface temperature (GMST) has increased during the last 100–150 years [3]. Stocker et al. [3] further states that each of the last three decades have successively been warmer at the earth's surface than the last.

The report uses a set of specific terms to indicate the likelihood of the assessments given in Table 2.1. For instance, in AR5 one can read that:

> It is also *virtually certain* that maximum and minimum temperatures over land have increased on a global scale since 1950.

From Table 2.1 it is clear that this means that the probability of this statement being true is evaluated to being in the range of 99–100%. While the quote from IPCC's AR5 is a nice demonstration of their usage of the terms to ensure consistency when treating uncertainties, it is also a quote worth to consider. Clearly, the international community of scientists agree that global warming is real, and that it constitutes a real problem.

2.1.1 Summary of key observations

As technology has been developed sensors have been put into the field, allowing for precise measurements to be made. Thus, at least since the 1970s there exists good quality datasets available to the climate researchers.

Table 2.1: Description of terms used to quantify likelihood in the technical summary of IPCC's fifth assessment report [3]. The terms are typeset in italics.

Term	Likelihood of outcome [%]
Virtually certain	99–100
Very likely	90–100
Likely	66–100
About as likely as not	33–66
Unlikely	0–33
Very unlikely	0–10
Exceptionally unlikely	0–1

Summing up the key observations during these decades shows that in the northern hemisphere we have *very likely* had the warmest 30-year period from 1983–2012 of the last eight centuries. Furthermore, it was *likely* the warmest period the last fourteen centuries [3]. Globally, it is *virtually certain* that the troposphere has warmed during the last 50–60 years, and that the stratosphere has cooled. The change in temperature is not only confined to the atmosphere. Stocker et al. [3] asserts that it is *virtually certain* that the upper part of the ocean, down to 700 m, have warmed in the period 1971–2010. In the longer perspective, they believe it *likely* warmed from 1870–1971.

In the Arctic, Stocker et al. [3] affirms with *very high confidence* that the extent of the sea ice has decreased in the period 1971–2012, and that the rate of change *very likely* was between 450 000–510 000 km^2. To put this in perspective, the area of Norway is 385 171 km^2, including Svalbard and Jan Mayen [4]. I.e. each decade the extent of Arctic sea ice is reduced with an area corresponding to at least 1.15 times the area of the kingdom of Norway.

One of the more troubling conclusions from the Technical Summary found in AR5 is that the Earth has been in radiative imbalance since at least about 1970 [3]. They declare it *virtually certain* that the Earth has gained substantial energy by radiation from the Sun entering the Earth's atmosphere, without a similar amount exiting.

One of the consequences of global warming is the potential for rising sea levels as the Antarctic and Greenland glaciers melts. AR5 asserts with *very high confidence* that glaciers all over the world are diminishing. For the last two decades the Antarctic ice sheet has been losing ice, and there is a *high confidence* that acceleration of outlet glaciers is to blame. To make matters worse, the current climate and glaciers are not in equilibrium, ensuring further future melting. The report states that even if the current temperature increase were to subside, the glaciers will continue to ebb.

This is in spite of trends towards, and observations of larger floods due to, heavier precipitation.

2.1.2 Greenhouse gases

Greenhouse gases (GHGs) like carbon dioxide, methane (CH_4), H_2O, nitrous oxide (N_2O) and halocarbons are gases that adsorb (and can emit) infrared radiation, and thus trap heat in the atmosphere by adsorbing and reemitting the radiation [3].

While both carbon dioxide and water (along with methane and nitrous oxide) are natural occurring, where water is the most abundant, carbon dioxide is the one receiving the attention. When burning fossil fuels, the hydrocarbon chains breaks down into CO_2 and H_2O (along with heat). Fossil fuels can be considered as chemical stable CO_2 containers; when it is extracted and consumed CO_2 is released into the atmosphere. By releasing the CO_2, the atmospheric concentration of CO_2 is increased, and the greenhouse effect increases as a consequence. The increased net radiative flux, or radiative forcing (RF) as it is known as [3], of all well-mixed greenhouse gas (WMGHG) was in 2011 estimated to be $(2.83 \pm 0.29)\,\mathrm{W\,m^{-2}}$, for CO_2 by itself the number is $(1.82 \pm 0.19)\,\mathrm{W\,m^{-2}}$ from the industrial era. Carbon dioxide on its own makes up for more than half of the RF. This makes CO_2 an important focus for reducing emissions in the effort to halt the global warming.

Again turning to Stocker et al. [3], the concentration of GHGs measured in 2011 exceed recorded concentrations from the past 800 000 years (stemming from polar ice core samples). It is estimated that the CO_2 emissions from fossil fuel use and cement production between 1750 and 2011 was $(375 \pm 30) \times 10^{15}$ g of carbon, where 1×10^{15} g of carbon is corresponds to 3.6675×10^{15} g of CO_2. If the emissions from land use is included the number rises to 555×10^{15} g carbon released, where $(240 \pm 10) \times 10^{15}$ g carbon accumulated in the atmosphere. The remainder re-adsorbed into the oceans or used by plants in photosynthesis and trapped, etc.

As the atmospheric concentration of CO_2 increases, the concentration in the oceans are bound to rise too. Stocker et al. [3] states that it is *very likely* that the total oceanic content of carbon increased from 1994 to 2010. As briefly mentioned in the introduction, the dissolution of CO_2 in water leads to a lowering of the pH. AR5 (and references therein) determines that the pH of the oceanic surface water has decreased by 0.1 since the beginning of the industrial era. Since pH is a logarithmic scale, the rather small decrease of 0.1 actually corresponds to a 26 % increase in H^+ concentration.

Methane is another greenhouse gas that has had increasing atmospheric concentrations during the industrial era. The concentration has increased from the 1750s where it was 722 ± 25 to 1803 ± 4 parts per billion (ppb) in 2011. Stocker et al. [3] asserts with *very high confidence* that the increase is caused by human activities. Methane atmospheric concentrations has had a period of little to no increase, but recently the concentrations has started to increase again. Consequently the RF increased by 2 % from fourth assessment report (AR4) to fifth assessment report, *very likely* making the RF from CH_4 larger than that of the halocarbons as a class in total.

2.2 Carbon capture and sequestration

As given above in subsection 2.1.2, CO_2 is the cause of more than 50 % of the radiative forcing. At the same time, the majority of CO_2 is released from use of fossil fuels. Since some of the worst polluters are coal power plants, which are large single source polluters, capturing and sequestrating the CO_2 currently released from these is a viable option.

Carbon capture

By capturing the GHGs, and CO_2 in particular, the rate of global warming can be slowed down. Capturing CO_2 can be done via different methods, and is usually categorized into three different branches of technology [5].

Post-combustion	CO_2 capture from flue gas after combustion. Can be done through amine-extraction processes.
Pre-combustion	Capture of carbon prior to combustion, usually through production of hydrogen gas (H_2) as an energy-carrier.
Oxy-combustion	Generation of high CO_2 concentration flue gas through combustion in an oxygen-rich atmosphere mixed with recycled flue gas.

The most common method, the *post-combustion* capture where the carbon dioxide is separated from from the flue gas, has the advantage that it can be retrofitted to existing coal power plants. However, there are several disadvantages such as low concentration of CO_2 in the flue gas (harder to separate out), and low pressure flue gas, which mandates the compression of CO_2 for pipeline transport and/or subsurface injection [5]. While CO_2 reaction with amines have been the traditional method of extraction, and is still being researched and improved on, there are several other emerging methods such as carbonate-based systems, aqueous ammonia, separation by membranes, capture by sorbents, adsorption in metal organic frameworks (MOFs), CO_2 reactions with enzymes and the use of ionic liquids [5]. While the future for post-combustion carbon capture may be promising, the disadvantages mentioned above are general and apply to all these systems.

Removal of the carbon prior to combustion is known as *pre-combustion* capture. The process works by gasification of the fuel under high temperature and pressure with the addition of oxygen. The result is synthesis gas (syngas), in essence consisting of carbon monoxide (CO) and H_2. By adding steam to the syngas in a shift converter the CO reacts with the H_2O-gas and turns into CO_2 and H_2. Prior to combustion of the hydrogen gas the carbon dioxide has to be separated out. Given the difference in physical size and chemical properties, membrane separation of H_2 and CO_2 is, if not exactly an easy process, at least manageable. The advantage of pre-combustion methods is that the exhaust from the subsequent combustion of the H_2 is pure H_2O. Furthermore, the syngas-process is a high-pressure process, meaning that the need for increasing the CO_2 pressure prior to pipeline transport/injection is reduced. The higher concentrations of CO_2, compared to post-combustion concentrations, also makes for easier separation. The disadvantage is cost of the system and the inability of retrofitting, which limits its use to new plants [5].

The third option, *oxy-combustion*, relies on burning the fuel in a very oxygen-rich atmosphere (above 95 %) mixed with recycled flue gas [5]. In this process the CO_2 concentration in flue gas is increased significantly, by the continuous recycling, to the point where it consist almost exclusively of CO_2 and H_2O, with traces contaminants. The advantages are the high concentration of CO_2 in the flue gas and that this technology can be retrofitted, much like the post-combustion technologies. However, there are several challenges with this technology. First, a high demand of oxygen for injection into the combustion process makes a on-site cryogenic oxygen-plant a prerequisite, for which the cost of operation may be formidable. Similarly to that of he post-combustion methods, the pressure of captured carbon dioxide is low which calls for compressors for obtaining the necessary pressure for transport or injection.

Sequestration

Carbon sequestration can be sorted into two main groups, biotic and abiotic sequestration. For the purposes of this text the focus will be exclusively on the managed abiotic carbon sequestration. Lal [6] lists four main methods of abiotic managed sequestration:

- Mineralization
- Oceanic injection
- Chemical scrubbing
- Geological sequestration

Chemical scrubbing can be the same process as the post-combustion amine extraction discussed above in subsubsection 2.2. However, in the carbon capture process, the amines (or carbon scrubbers in general) are usually regenerated, where the CO_2 is released from the absorbent. By choosing not to regenerate the absorbent the captured CO_2 remains absorbed, and as such it could conceivably be considered a sequestration method. Nonetheless, chemical scrubbing is usually only viewed as a part of the capture process due to the cost of absorbents, and will not be further discussed here.

Mineralization is an interesting process and one that inherently may be considered a part of many geological sequestration projects through for instance generation of calcite. Carbon sequestration by means of mineralization is the process of binding CO_2 to other elements such as calcium or magnesium, thus forming minerals, in this case calcite ($CaCO_3$) and magnesite ($MgCO_3$). Both of these are examples of mineral carbonation. Carbon dioxide mineralization is not limited to only these two processes, and several other reactions can occur. These are examples of natural processes, that takes place by themselves. The challenge lies in industrialization of the processes, by speeding up the slow rates of reaction [6]. Accelerating the rate of reactions can be done by increasing temperature and pressure, but that has its own cost in form of energy input.

It is well-known that oceans cover 71 % of the earth's surface. The large bodies of water makes oceanic injection of CO_2 a tempting prospect. According to Lal [6], the initial proposals were made in the late 1970s. It is prudent to note that the AR5 asserts that the oceanic pH has decreased since the start of the industrial era, and that dissolution of carbon dioxide is the likely cause of this decrease. With that in mind, oceanic injection of CO_2 may not be all that clever [6], and could have some detrimental consequences for the ecosystem.

The most promising technique for carbon sequestration is that of geological injection. Geological injection of CO_2 has been commercially utilized since 1996 in Statoil's Sleipner Vest CO_2 disposal project [7]. In this project CO_2 had to be removed from the natural gas produced from the wells to meet the customer product specifications. Releasing the carbon dioxide into the atmosphere would have incurred significant expenses due to the CO_2-quota system. Thus, from a business point of view, it made economical sense to inject the captured CO_2 into the Utsira formation.

Carbon dioxide has further uses within the oil and gas sector. Injection of CO_2 in oil reservoirs is an effective method of enhanced oil recovery (EOR). The injected CO_2 can work as an highly effective solvent for small hydrocarbons and aromatics [8], and lower the viscosity of the solution. With lower viscosity, the hydrocarbons can achieve higher flow-rates which in turn can result in increased production. Similarly, injection of CO_2 into deep subsurface coal seams with concurrent natural gas production can displace CH_4 and increase production while the CO_2 remains trapped. The benefit of this method is to offset the cost of carbon sequestration by the energy gained from the CH_4. Several field tests were successfully carried out using variations of this technique in the mid 1990s in the San Juan Basin (non-exhaustive list) [8].

A third candidate for geological sequestration is injection in deep saline aquifers of which are widespread and thus lessens the distance of transportation. In the deep saline aquifers CO_2 can be trapped in different manners. Under the right conditions CO_2 can form its own gas phase from the brine, and when prevented from rising higher in the formation due to cap-rock (or a low permeability layer), the CO_2 is constrained to the natural hydrodynamic gradient [8]. This is known as *hydrodynamic trapping*. Carbon dioxide can also dissolve into the brine and become *solubility trapped*. Dissolving CO_2 into brine results in lowering of the pH. Calcite, for instance, dissolves in acidic solutions. The potential for dissolution of the mineral matrix, poses some potential problems. The worst case scenario is weakening of the cap-rock, or increase in the permeability in low permeability zones, allowing for migration of CO_2 to the surface. Dissolution with subsequent precipitation or carbonization of minerals may change the permeability in near-injection well areas. If the permeability is reduced, higher injection-pressure might be necessary to inject at the same rate, with the potential for inducing fractions in the mineral matrix. Finally, injected carbon dioxide may be subjected to *mineral trapping*. Dissolved CO_2 can undergo an chemical reaction with cations and form mineral particles that precipitate from the solution. While the side-consequences as described above may be undesirable, mineral trapping is the most stable underground trapping.

To conclude, there are many methods of carbon sequestration. Subsurface sequestration seems not only to be the most promising, but is also a proven method.

2.3 Pipeline transport challenges

For any carbon sequestration to take place, pipeline transport of some kind is almost a given necessity. Assuming subsurface injection, be it in a deep coal seam, saline aquifer, depleted hydrocarbon reservoir or even as part of an EOR project, the CO_2 has to be transported to the injection site.

Pipeline transport is by no means a new technology. Hydrocarbons as gas, liquid and multiphase fluids, have been successfully transported through pipelines over long distances for quite a substantial time. Prior to hydrocarbon transport, water and sewer-systems were (and still are) highly dependent on effective pipeline distribution systems. Despite pipeline transport being a proven and well-known technology, both old and new challenges arises and must be handled when dealing with CCS. Several challenges have to be considered, evaluated and solved prior to effective pipeline transport of carbon dioxide from capture-site to injection-site. In no particular order, some of the challenges are:

- Erosion
- Corrosion
- Hydrate formation

Erosion

In Norway, carbon sequestration will very likely be carried out by injection into depleted hydrocarbon reservoirs, saline aquifers or as part of enhanced oil recovery. Thus, the pipelines will have to be put on the seafloor for efficient transport to take place. This further complicates some of the problems. Erosion, where solid particle within the fluid phase transported in the pipeline works as an abrasive, can over time weaken pipeline wall to the point of failure. Such a failure would incur considerable cost of repair, not to mention the downtime where CO_2 would likely have to be released to the atmosphere rather than injected due to no viable alternative transportation. Fortunately, in most capture-scenarios there are few sources for particulates to enter the fluid stream and as such, while the consequences may be severe, the likelihood of this failure-mode occurring is not very high.

Corrosion

More problematic is the issue of corrosion. Flue gases inherently contains H_2O which in contact with iron pipeline walls readily cause corrosion. The fact that CO_2 is present as well does nothing to improve on the situation, as CO_2 can result in very high corrosion rates when dissolved in water [9]. Corrosion of the pipeline walls can lead to severe weakening to the point where the structure no longer can withstand the high internal pressure. CO_2 corrosion is dependent on a multitude of parameters. Among these are T, p, pH and water wetting [9]. In a pipeline the temperature is usually beyond the operator's control and is given by the ambient temperature of the surroundings. With pressure there can be some leeway, but it has to be sufficiently high for injection to occur, while being low enough to avoid unintentional fracturing of the rock matrix. In the field this means that both T and p are more or less fixed due to the environment and are not parameters that can be tuned to reduce the impact of corrosion. The pH has a dual effect on corrosion. It affects the electrochemical reactions and can accelerate or decelerate the rate of corrosion. At higher pH, the solubility of ferrous ion (Fe^{2+}) is reduced. The reduction of Fe^{2+}–solubility can accelerate the precipitation of siderite ($FeCO_3$) that can form a protective film on the surface, decelerating further corrosion. Again it is prudent to mention that CO_2 dissolved in water lead to a lower pH and as such may prevent the precipitation of $FeCO_3$. Uncoated carbon steel or mild iron surfaces are water wetting surfaces. The presence of both a water film and CO_2 is necessary for CO_2–corrosion, but can also result in a transparent corrosion surface film which is protective against corrosion. Despite the protection, corrosion failures, predominantly due to CO_2–corrosion, account for $\sim$25 % of all safety incidents in the oil and gas industry [9].

Hydrate formation

Pipeline surfaces, whether corroded or not, are water wetting surfaces. This makes the surfaces susceptible to adsorption of a thin water film, if water is present in the fluid stream. Clathrates, or gas hydrates, has long been a challenge for the oil and gas industry. Gas hydrates exists in several forms, but are essentially networks of hydrogen-bonded water molecules that form cavities which are stabilized by guest molecules. CO_2 is one of the guest molecules capable of stabilizing the cavities and thus contribute to hydrate formation. In fact, CO_2 has proven to be a more aggressive hydrate former than, for instance, CH_4. The presence of H_2O and CO_2 makes hydrate formation plausible if the thermodynamic conditions are such that hydrates will be stable. The low ambient temperature on the seafloor are within the hydrate stability zone for CO_2–hydrates. As are the high pressures usually associated with pipeline transport [10]. With both temperature and pressure within the hydrate stability zone, hydrate formation can present a serious problem for future CO_2–pipelines. It is well-known within the oil and gas industry that plugging of pipelines due to hydrate formation presents challenges both in the form of accidents (health, safety and the environment (HSE)–risk) and the staggering costs associated with shutting down the pipeline and rectifying the issue. Thus, the potential for hydrate formation under such conditions surely need more research to ensure prior knowledge of proper operating conditions and hydrate formation risks.

2.4 Gas dehydration

Water has to be present for hydrates to form. Its presence is also a major contributor to corrosion. Without water there is no molecules to form the hydrogen bonded network of cavities which trap the guest molecules in hydrates. Since carbon dioxide is a guest molecule and surely present in a CO_2–pipeline, water removal from the gas stream is the only viable option for hydrate prevention through removal of hydrate constituents. Water removal can also be important in preventing corrosion.

Removing water from a gas can be carried out by different means such as absorption, adsorption, condensation or selectively permeable membranes. The oil and gas industry has extensive knowledge of absorption of water from gas streams using glycols (for instance tri-ethylene glycol (TEG)). Here the gas stream is fed through an absorber where the water in the gas comes into contact with the glycols and is absorbed into the liquid glycol phase, which is circulated through a stripping process where the absorbed water is boiled out of the TEG. The regenerated TEG is then pumped back to the absorber. Generally, absorption by glycols are used for bulk removal of water down to approximately 60 parts per million by volume (ppmV) [11], but it is possible to lower the water content to as little as a few ppmV [12]. As a side note there are some cases where glycols are injected into critical parts of gas processing plants without a separate dehydration unit or in critical parts prior to dehydration units. That is, however, considered a method of reducing hydrate formation risk, and not as a dehydration method.

Condensation by cooling the gas is another option. By, for instance, utilizing the Joule-Thompson effect, water can condensate out from the gas when the pressure is lowered. The liquid water is then removed from the gas stream. The disadvantage is that the dehydrated gas stream will have to undergo re-compression before pipeline transport. In a CCS scenario, the flue gas is likely already as atmospheric pressure, thus requiring the flue gas to be compressed twice.

The third option is dehydration by adsorption. Here silica gels and molecular sieves are often used. Molecular sieves, such as LTA zeolites, can selectively allow water to enter into the cavities and adsorb there, while blocking access to other molecules. While molecular sieves can achieve a dry gas with very low water content, a low as 0.03 ppmV [12], they are more expensive to install, require batch operation, the adsorbent must be replaced from time to time, and the regeneration process requires more energy in form of added heat than a glycol absorber/stripper-plant. The required energy depends of course on the adsorption characteristics of the zeolite in question and the required degree of regeneration.

However, even though molecular sieves are susceptible to attack by acids, they perform better with sour gas than glycols. The main reason being that for instance LTA-4A can adsorb both CO_2 and H_2S, thus removing the sour gas components from the gas stream. This is an advantage when considering the damage that can be incurred by corrosion. When dealing with a CO_2-pipeline LTA-4A is likely not a good choice for a molecular sieve for dehydration due to CO_2 being capable of entering the cavities. In that case LTA-3A may be a better choice, as CO_2 has a harder time entering the cavities due to the larger counter-ions blocking the entrances. More on this in subsubsection 4.1.2, Simulation constituents and details, which deals specifically with zeolites.

Chapter 3: Theory of molecular simulation

3.1 Molecular dynamics

Alder and Wainwright [13] stated in the abstract of their paper that "A method is outlined by which it is possible to calculate exactly the behavior of several hundred interacting classical particles." This is in essence molecular dynamics (MD) described in a sentence. The limits on how *exactly* the behavior can be calculated depends in a large degree on the choice of force fields and computational methods. As with most other model-based methods in physics, as well as pretty much every other branch of science, it has its short-comings. MD is, nonetheless, a very powerful tool for generating molecular trajectories, statistical information and mapping out portions of phase space.

3.1.1 Statistical mechanics

Statistical mechanics is a branch of physics that connects the interactions and momenta of particles to thermodynamic observables, or variables. It has been widely successful in explaining physical observable phenomenons from the atomistic origin. Statistical mechanics is also the theoretical basis for molecular dynamics, in the way statistical mechanics couples the microscopic fluctuations, configurations and motions to macroscopic observable properties.

In thermodynamics we observe the macroscopic system and the corresponding macroscopic properties. For a macroscopic system in a given macrostate, there is an exceedingly large number of corresponding microstates. The microstates are defined by, and constrained to, the macroscopic variables. An isolated system has a fixed number of particles (N), a fixed volume (V), and a certain amount of energy (E). The variables N, V and E define the constraints on the system, and the corresponding microstates. Every microstate belonging to the macrostate thus have to have the same number of particles, total energy and volume.

Ensembles in statistical mechanics

In statistical mechanics there are several ensembles. The microcanonical, canonical and grand canonical ensembles are the most known. For each of these ensembles there is a set of fixed variables, the macroscopic thermodynamic observables that define the constraints on the system (see Table 3.1).

For each of the ensembles a partition function can be derived. The partition functions are crucial in statistical mechanics as they hold a wealth of information about the system. They are also the path to the thermodynamic quantities.

Table 3.1: Ensembles and partition functions in statistical mechanics [14, pp. 78, 138, 268]. $\mathcal{H}$ is the Hamiltonian, M_N the microcanonical normalization factor and C_N the canonical normalization factor.

Ensemble	**Variables**	**Partition function**
Microcanonical	N, V, E	$\Omega(N,V,E) = M_N \int dx\, \delta(\mathcal{H}(x) - E)$
Canonical	N, V, T	$Q(N,V,T) = C_N \int dx\, e^{-\beta\mathcal{H}(x)}$
Grand canonical	μ, V, T	$\mathcal{Z}(\mu,V,T) = \sum_{N=0}^{\infty} e^{\beta\mu N} Q(N,V,T)$

For instance, in the simple case of the microcanonical ensemble it is possible to define $\Omega(N,V,E)$ as the number of microstates belonging to the macrostate such that:

$$\Omega(N,V,E) = \text{number of microstates with } N,V \text{ and } E \text{ in } [E, E-\delta E]. \tag{3.1}$$

If we assume that all microstates are equally probable at thermodynamic equilibrium, then

$$P_\nu = \frac{1}{\Omega(N,V,E)} \tag{3.2}$$

is the probability, P_ν, of being in microstate ν. The entropy is then defined as

$$S = k_B \ln \Omega(N,V,E), \tag{3.3}$$

where, S is the entropy and k_B is Boltzmann's constant.

Returning to Table 3.1, each ensemble has a set of fixed variables. For the microcanonical ensemble the system, with fixed number of particles, volume and energy, is completely isolated. There is no change in volume, no particles may enter or leave the system nor may energy. The canonical ensemble on the other hand has fixed temperature instead of energy. This difference allow for energy to be exchanged with the surroundings, keeping the temperature constant. It is usual to visualize this as if the system was connected to, or lowered into, a heat bath with infinite potential. With the grand canonical ensemble the concept is somewhat more complex. With the chemical potential, volume and temperature is fixed, the system can exchange matter with its surroundings. Thus, mass, energy and pressure of the system may fluctuate as matter enters or leaves the system, as long as the chemical potential, volume and temperature remain fixed. It is in connection with a reservoir containing an infinite large number of particles.

Phase space

The classical Hamiltonian is given as the sum of potential and kinetic energy in the system,

$$\mathcal{H}(\mathbf{q},\mathbf{p}) = U(\mathbf{q}_1,\ldots,\mathbf{q}_N) + \sum_{i=1}^{N} \frac{\mathbf{p}_i^2}{2m_i}, \tag{3.4}$$

where for particle i $\mathbf{q}_i$ is the position, $\mathbf{p}_i$ is the momentum and m_i is the mass. Note that the potential energy is a function of the positions only, while the kinetic energy is a function of the momenta. It is usual to talk about them belonging to *configurational space* and *momentum space* which are the vector spaces spanned by the positions and momenta, respectively. For a system of N particles, phase space – the space spanned by both positions and momenta – the points in phase space are then defined by:

$$\left(q^N, p^N\right) := \left(\mathbf{q_1}, \mathbf{q_2}, \ldots, \mathbf{q_N}; \mathbf{p_1}, \mathbf{p_2}, \ldots, \mathbf{p_N}\right) \tag{3.5}$$

Phase space is thus a $6N$ dimensional space, encompassing all possible positions and momenta. In the microcanonical ensemble the constraints (N,V,E) limit the possible points for the given system in phase space to a complex surface. If we were to follow the time-evolution of such a system, the trajectory would trace a path on that surface.

Ergodicity

A concept in statistical mechanics is that of *ergodicity*. The general idea is that if we follow the time-evolution (or the trajectory) for a sufficiently long enough time, we will eventually pass through all points on the phase-space surface (constrained by the ensemble variables), or at least close to. Mathematically we have that the ensemble average, $\langle A \rangle$, is equal to the time-average, $\overline{A(t)}$, when the time goes towards infinity (see Eq. (3.6)).

$$\lim_{t \to \infty} \overline{A(t)} = \langle A \rangle \tag{3.6}$$

This hypothesis is what we are exploiting in MD. Based on the hypothesis one makes the assumption that the systems partition function is sampled proportional to the ensemble's partition function, and the systems observables are approximating the ensemble observables. Key for this to be valid are that a proper force field is used and that the observation period is sufficiently long. In the context of molecular dynamics simulations this is somewhat more complicated as the user, and indeed the implementation itself, may disrupt the system or sampling.

3.1.2 Governing equations

The design of MD is to model the interactions of particles, such as atoms or molecules, using Newton's laws. By assigning potentials to atoms, the potential energy $U(\mathbf{r})$ between two atoms separated by a distance $|\mathbf{r}|$ can be calculated. The force acting on the atoms can then be found using Eq. (3.7)

$$\mathbf{F}(\mathbf{r}) = -\nabla U(\mathbf{r}), \tag{3.7}$$

where $\mathbf{F}$ is the resulting force vector, U is the potential energy and $\mathbf{r}$ is the vector from atom i to atom j. By summing up all contributions for every particle the acceleration for each and every particle is then calculated from Newton's second law.

To obtain the potential energy, the force field (see section 3.2) comes into play. Force fields contain the means, in form of functional forms and parameters, to calculate the potential energy of the particles. While the algorithms of and in MD are important, the choice of a force field may be crucial to succeed.

3.1.3 Integration of motion

From application of the force fields one get the potential energy. By Equation 3.7 and Newton's second law one obtain the acceleration. But to advance the system in time an integration algorithm for the particles is needed. Luckily, of these there are many. There is the Verlét algorithm, velocity Verlét, leapfrog and all the Runge-Kutta methods. Some are more stable than others, some are computationally less costly than others and some are more convenient than others. In the end, they are supposed to solve the same task, advance the system in time.

Verlét algorithm

One of the simplest algorithms, and perhaps best known, is the Verlét algorithm. The derivation of this algorithm is fairly easy. Write down the Taylor expansions of the position of particle i, $\mathbf{q}_i$ for time $(t \pm \Delta t)$

$$\mathbf{q_i}(t+\Delta t) = \mathbf{q_i}(t) + \left(\frac{d\mathbf{q_i}}{dt}\right)_t \Delta t + \frac{1}{2}\left(\frac{d^2\mathbf{q_i}}{dt^2}\right)_t (\Delta t)^2 + \dots \tag{3.8}$$

$$\mathbf{q_i}(t-\Delta t) = \mathbf{q_i}(t) - \left(\frac{d\mathbf{q_i}}{dt}\right)_t \Delta t + \frac{1}{2}\left(\frac{d^2\mathbf{q_i}}{dt^2}\right)_t (\Delta t)^2 + \dots \tag{3.9}$$

Add Equation 3.8 and Equation 3.9, and with some rearranging one get

$$\mathbf{q_i}(t+\Delta t) = 2\mathbf{q_i}(t) - \mathbf{q_i}(t-\Delta t) + \left(\frac{d^2\mathbf{q_i}}{dt^2}\right)_t (\Delta t)^2, \tag{3.10}$$

which is the Verlét algorithm. One of its interesting features, which is somewhat hard to see here since this derivation stopped the Taylor expansion after the second order, is that the third order expansions cancels, just like the first order (the velocity) did. Thus the truncation error of this algorithm is to the fourth order. The disadvantage is that the velocity disappeared. The latter can easily be rectified by

$$\mathbf{v_i}(t) = \frac{\mathbf{q_i}(t+\Delta t) - \mathbf{q_i}(t-\Delta t)}{2\Delta t}, \tag{3.11}$$

or by using the slightly different velocity Verlét algorithm.

Leapfrog algorithm

The leapfrog algorithm is another method. This method does return both the position and velocity. However, at each point in time one only has the position *or* the velocity. This may again easily be corrected along the lines of Equation 3.11. In the leapfrog algorithm one start with the Taylor expansions over the velocities at time $\left(t \pm \frac{\Delta t}{2}\right)$,

$$\mathbf{v_i}\left(t+\frac{\Delta t}{2}\right) = \mathbf{v_i}(t) + \left(\frac{d\mathbf{v_i}}{dt}\right)_t \frac{\Delta t}{2} + \frac{1}{2}\left(\frac{d^2\mathbf{v_i}}{dt^2}\right)_t \left(\frac{\Delta t}{2}\right)^2 + \dots \tag{3.12}$$

$$\mathbf{v_i}\left(t-\frac{\Delta t}{2}\right) = \mathbf{v_i}(t) - \left(\frac{d\mathbf{v_i}}{dt}\right)_t \frac{\Delta t}{2} + \frac{1}{2}\left(\frac{d^2\mathbf{v_i}}{dt^2}\right)_t \left(\frac{\Delta t}{2}\right)^2 + \dots \tag{3.13}$$

These equations are then subtracted from each other and rearranged to yield

$$\mathbf{v_i}\left(t+\frac{\Delta t}{2}\right)=\mathbf{v_i}\left(t-\frac{\Delta t}{2}\right)+\left(\frac{d\mathbf{v_i}}{dt}\right)_t\Delta t+\ldots, \tag{3.14}$$

which is the velocity part of the leapfrog algorithm. Repeating the procedure for the positions, but now for time $\left(\left[t+\frac{\Delta t}{2}\right]\pm\frac{\Delta t}{2}\right)$ and one get

$$\begin{aligned}\mathbf{q_i}\left(t+\frac{\Delta t}{2}+\frac{\Delta t}{2}\right)=&\,\mathbf{q_i}\left(t+\frac{\Delta t}{2}\right)\\&+\left(\frac{d\mathbf{q_i}}{dt}\right)_{t+\frac{\Delta t}{2}}\left(\frac{\Delta t}{2}\right)+\frac{1}{2}\left(\frac{d^2\mathbf{q_i}}{dt^2}\right)_{t+\frac{\Delta t}{2}}\left(\frac{\Delta t}{2}\right)^2+\ldots\end{aligned} \tag{3.15}$$

and

$$\begin{aligned}\mathbf{q_i}\left(t+\frac{\Delta t}{2}-\frac{\Delta t}{2}\right)=&\,\mathbf{q_i}\left(t+\frac{\Delta t}{2}\right)\\&-\left(\frac{d\mathbf{q_i}}{dt}\right)_{t+\frac{\Delta t}{2}}\left(\frac{\Delta t}{2}\right)+\frac{1}{2}\left(\frac{d^2\mathbf{q_i}}{dt^2}\right)_{t+\frac{\Delta t}{2}}\left(\frac{\Delta t}{2}\right)^2+\ldots\end{aligned} \tag{3.16}$$

subtracting Equation 3.16 from Equation 3.15 and the position part of the leapfrog algorithm come out as

$$\begin{aligned}&\mathbf{q_i}\left(t+\frac{\Delta t}{2}+\frac{\Delta t}{2}\right)-\mathbf{q_i}\left(t+\frac{\Delta t}{2}-\frac{\Delta t}{2}\right)=\\&\mathbf{q_i}(t+\Delta t)-\mathbf{q_i}(t)=\Delta t\left(\frac{d\mathbf{q_i}}{dt}\right)_{t+\frac{\Delta t}{2}}+\ldots,\end{aligned} \tag{3.17}$$

which by some rearranging and substitution becomes the usual equation for the positions in the leapfrog algorithm:

$$\mathbf{q_i}(t+\Delta t)=\mathbf{q_i}(t)+\mathbf{v_i}\left(t+\frac{\Delta t}{2}\right)\Delta t+\ldots. \tag{3.18}$$

As one now easily can see, the velocities are calculated at times $t+\frac{\Delta t}{2}$, with positions calculated at times $t+\Delta t$. This is the gist of the name "leapfrog", where the velocities leaps over the positions and vice versa.

3.1.4 Periodic boundary conditions

In molecular dynamics and scientific computation in general, a significant amount of effort goes into making the code, computation or application as efficient as possible. periodic boundary conditions (PBC) is one of the methods that can be utilized to simulate a system of infinite size while keeping a low number of actual particles. It is also a method that prevents the system from being dominated by the influence of particles

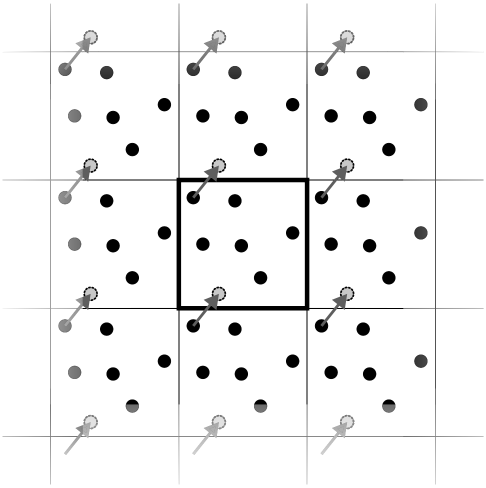

Figure 3.1: Illustration of periodic boundary conditions. The central box is here considered to be the simulation box, surrounded by copies of itself. When a particle, here indicated by a black circle, leaves the simulation box and enters a neighboring box, another particle, gray, which is in principle the same as the previous black particle, enters from the other direction.

constantly colliding with walls of the simulation box. This allows for simulation of bulk properties, even in a smaller system with limited number of particles.

The general concept is quite simple and is illustrated in two dimensions in Figure 3.1. When a particle, visualized as circles in Figure 3.1, moves outside the simulation box it reenters from the opposite side. This can be considered as if the particle moves into another box, and that a new particle enters the simulation box from a third box. In effect, one obtains a seemingly infinite simulation system, free from wall effects, with constant number density, capable of reproducing bulk properties.

3.1.5 Electrostatic interactions in periodic systems

As mentioned in subsubsection 3.2.2, Ewald summation methods are often used to calculate the long-range electrostatic interactions in periodic systems. These methods are employed as conventional methods, i.e.: using Coulomb's law, has a poor computational performance. If one wants to increase the performance, the introduction of a cut-off distance is required, with the then added inaccuracy.

In Ewald summation methods, here in the flavor of the smooth particle mesh of Essmann et al. [15], the contributions to the electrostatic potential energy is divided into three terms. These are the direct contribution Equation 3.19, which is calculated in normal space, the reciprocal contribution Equation 3.20, calculated in reciprocal space and the correction term Equation 3.21 which corrects for both intra-molecular interactions and self-interactions.

$$U_{dir} = \frac{1}{2}\sum_{n}^{*} \frac{q_i q_j \, erfc(\beta|\mathbf{r}_i - \mathbf{r}_j + \mathbf{n}|)}{|\mathbf{r}_i - \mathbf{r}_j + \mathbf{n}|} \tag{3.19}$$

$$U_{rec} = \frac{1}{2\pi V} \sum_{\mathbf{m}\neq 0} \frac{\exp(-\pi^2\mathbf{m}^2/\beta^2)}{\mathbf{m}^2} S(\mathbf{m})S(-\mathbf{m}) \tag{3.20}$$

$$U_{corr} = -\frac{1}{2} \sum_{(i,j)\in M} \frac{q_i q_j\, erf(\beta|\mathbf{r}_i - \mathbf{r}_j|)}{|\mathbf{r}_i - \mathbf{r}_j|} - \frac{\beta}{\sqrt{\pi}} \sum_{i=1}^{N} q_i^2 \tag{3.21}$$

In Equation (3.19)–(3.21) $erf()$ and $erfc()$ is the error function and the complementary error function, respectively, β is the Ewald coefficient and $\mathbf{n}$ is the periodic image vector. The Equation 3.21 is easy to calculate, given that one has the list of "masked pairs", M. As the interesting parts are in the reciprocal contributions (Equation 3.20) the section below, subsubsection 3.1.5, is devoted to solving that equation.

To sum it up, the total electrostatic potential energy is then given as:

$$U = U_{dir} + U_{rec} + U_{corr}. \tag{3.22}$$

Smooth particle mesh Ewald summation

The equations and formalism below is based on the work of Essmann et al. [15]. It is included here as it was necessary to develop a utility to build a map of the electrostatic potential energies. The utility used the smooth particle mesh Ewald summation method.

Let: $\mathbf{a}_\alpha$, where $\alpha = 1,2,3$, form the edges of a unit cell. $\mathbf{a}_\alpha^*$ is the conjugate reciprocal vectors defined by $\mathbf{a}_\alpha^* \cdot \mathbf{a}_\beta = \delta_{\alpha\beta}$ for $\alpha,\beta = 1,2,3$, where $\delta_{\alpha\beta}$ is the Kronecker delta. The unit cell is filled with N point charges $q_1, q_2, \ldots, q_N$, with positions $\mathbf{r}_1, \mathbf{r}_2, \ldots, \mathbf{r}_N$. Corresponding fractional coordinates $s_{\alpha i}$, for point charge i is given by $s_{\alpha i} = \mathbf{a}_\alpha^* \cdot \mathbf{r}_i$. Since the point charges interact not only with the neighboring charges, but also with all their periodic images as well (but not itself or its image), a vector $\mathbf{n} = n_1\alpha_1 + n_2\alpha_2 + n_3\alpha_3$, where the integers n_1, n_2, n_3 cannot be all 0 at the same time, give the position of the periodic images. Finally we need to define the reciprocal lattice vectors $\mathbf{m} = m_1\alpha_1^* + m_2\alpha_2^* + m_3\alpha_3^*$, where m_1, m_2, m_3 are integers that cannot all be 0 at the same time.

With the definitions above now in place, the structure factor $S(\mathbf{m})$ in eq. (3.20) is defined as

$$\begin{aligned} S(\mathbf{m}) &= \sum_{j=1}^{N} q_j \exp(2\pi i \mathbf{m} \cdot \mathbf{r}_j) \\ &= \sum_{j=1}^{N} q_j \exp(2\pi i [m_1 s_{1j} + m_2 s_{2j} + m_3 s_{3j}]). \end{aligned} \tag{3.23}$$

We define the three positive integers, K_1, K_2, K_3. Then for any point charge, a scaled fractional coordinate is defined by $u_\alpha = K_\alpha \mathbf{a}_\alpha^* \cdot \mathbf{r}$. Since periodic boundary conditions are used, one can assume that $0 \leq u_\alpha < K_\alpha$. Then the exponentials from (3.23) can be expressed as:

$$\exp(2\pi i \mathbf{m} \cdot \mathbf{r}) = \exp(2\pi i \frac{m_1 u_1}{K_1}) \cdot \exp(2\pi i \frac{m_2 u_2}{K_2}) \cdot \exp(2\pi i \frac{m_3 u_3}{K_3}). \tag{3.24}$$

Using Cardinal B-splines, the exponentials on the right hand side of equation (3.24) can be approximated as

$$\exp(2\pi i\frac{m_i u_i}{K_i}) \approx b_i(m_i)\sum_{k=-\infty}^{\infty} M_n(u_i-k)\cdot\exp(2\pi i\frac{m_i}{K_i}k), \tag{3.25}$$

where M_n is the Cardinal B-spline defined by

$$M_2(u) = \begin{cases} 0 & \text{for } u<0 \text{ or } u>2 \\ 1-|u-1| & \text{for } 0\leq u\leq 2 \end{cases}, \tag{3.26}$$

and

$$M_n(u) = \frac{u}{n-1}M_{n-1}(u) + \frac{n-u}{n-1}M_{n-1}(u-1), \tag{3.27}$$

for any spline order $n>2$. The function $b_i(m_i)$ in equation (3.25) is now given by

$$b_i(m_i) = \exp(2\pi i(n-1)m_i/K_i)\times\left[\sum_{k=0}^{n-2} M_n(k+1)\exp(2\pi i m_i k/K_i)\right]. \tag{3.28}$$

We define two new arrays:

$$B(m_1,m_2,m_3) = |b_1(m_1)|^2\cdot|b_2(m_2)|^2\cdot|b_3(m_3)|^2, \tag{3.29}$$

where $b_i(m_i)$ is given by equation (3.28), and

$$C(m_1,m_2,m_3) = \frac{1}{\pi V}\frac{\exp(-\pi^2\mathbf{m}^2/\beta^2)}{\mathbf{m}^2}, \tag{3.30}$$

for $\mathbf{m}\neq 0$, with $C(0,0,0)=0$. Note that $\mathbf{m}$ is redefined in the definition of $C(m_1,m_2,m_3)$ as $\mathbf{m} = m_1'a_1^* + m_2'a_2^* + m_3'a_3^*$, where $m_i' = m_i$ for $0\leq m_i\leq K/2$ and $m_i' = m_i - K_i$ elsewhere. With all this in place, the pair potential θ_{rec} is given by the forward Fourier transform of $B\cdot C$, i.e. $\theta_{rec} = F(B\cdot C)$. At this point the only part missing is the "charge grid array"

$$\begin{aligned} Q(k_1,k_2,k_3) = \sum_{i=1}^{N}\sum_{n_1,n_2,n_3} & q_i\, M_n(u_{1i}-k_1-n_1K_1) \\ & \times M_n(u_{2i}-k_2-n_2K_2) \\ & \times M_n(u_{3i}-k_3-n_3K_3). \end{aligned} \tag{3.31}$$

Finally the approximate reciprocal energy is calculated as

$$\begin{aligned} \tilde{U}_{rec} = & \frac{1}{2\pi V}\sum_{m\neq 0}\frac{\exp(-\pi^2\mathbf{m}^2/\beta^2)}{\mathbf{m}^2}B(m_1,m_2,m_3) \\ & \cdot F(Q)(m_1,m_2,m_3)F(Q)(-m_1,-m_2,-m_3) \\ = & \frac{1}{2}\sum_{m_1=0}^{K_1-1}\sum_{m_2=0}^{K_2-1}\sum_{m_3=0}^{K_3-1} Q(m_1,m_2,m_3) \\ & \cdot(\theta_{rec}\star Q)(m_1,m_2,m_3), \end{aligned} \tag{3.32}$$

where $\theta_{rec} \star Q$ denotes the convolution of θ_{rec} and Q.

3.1.6 Temperature control

Molecular dynamics natural ensemble is the micro-canonical ensemble, i.e. constant N, V and E. For comparison with experimental data this is inconvenient as most experiments are performed in the canonical ensemble with constant N, V and T. Thus it is desirable to run simulations with a constant .

Thermostatting in MD simulations can be achieved through different methods, from the simple velocity scaling to the more complex methods such as Andersen thermostatting [16] or the Nosé-Hoover thermostat [17, 18]. Temperature is a measure of the velocity of particles through the well known relation

$$\frac{1}{2}mv^2 = \frac{3}{2}k_BT, \tag{3.33}$$

where m is the mass, v is the velocity and k_B is Boltzmann's constant. It's through this mechanism that the thermostats work. For the simple case of velocity scaling the velocity would be scaled up or down to a match a set system temperature. To avoid excessive system disturbance the velocities are usually only scaled when the measured temperature deviates by a set limit from the temperature of interest. While velocity scaling is an easy approach to simulations with constant temperature it is not a good approach. The method fails to generate the canonical partition function and the action of scaling the velocity makes phase space trajectories discontinuous.

A better method is to use the Andersen or Nosé-Hoover thermostats. Andersen's method relies on stochastic collisions imparting momenta to the particles, one particle at the time. Still, this has the disadvantage of making the phase space trajectories discontinuous whenever a particle experience such an event. The Nosé-Hoover thermostat does not make the trajectories discontinuous. It works by expanding the systems Hamiltonian by adding an additional degree of freedom;

$$\hat{\mathcal{H}}_{Nosé} = \phi(\mathbf{q}) + \sum \frac{\mathbf{p}^2}{2ms^2} + (X+1)\, k_bT \ln s + \frac{p_s^2}{2Q}, \tag{3.34}$$

where $\mathbf{q}$ is the position and $\mathbf{p}$ the momenta. The variable s is a time-scale variable, originally used by Nosé [17] to scale time, and p_s its coupled momentum [18]. Q behaves as a *virtual* mass for the variable s, and has dimensions $energy \cdot time^2$ [17].

Now, the Nosé thermostat as it was proposed had a disadvantage. It relied on scaling time. For MD simulations, where average quantities and properties, and more importantly time-average quantities and properties may be of interest, variable time is an inconvenience. Thus, Hoover [18] improved somewhat on Nosé's formulation and simplified the resulting equations of motion such that

$$\begin{aligned} \dot{\mathbf{q}} &= \frac{\mathbf{p}}{m}, \quad \dot{\mathbf{p}} = \mathbf{F}(\mathbf{q}) - \zeta \mathbf{p} \\ \dot{\zeta} &= \frac{\left[\sum \frac{\mathbf{p}^2}{m} - Xk_BT\right]}{Q}, \end{aligned} \tag{3.35}$$

where ζ is the thermodynamic friction coefficient [18]. The parameter X should be equal to the number of independent degrees of freedom in $\mathbf{q}$ and $\mathbf{p}$. Note that Equation 3.35 does no longer rely on time-scaling and are easier implemented in MD software.

3.1.7 Free energy calculations

The work in this thesis entailed calculating chemical potential of different species. As the chemical potential is not a natural variable/quantity in MD simulations this required some additional effort.

There are, as usual in the world of MD, multiple methods of estimating chemical potential. Of the more known methods are thermodynamic integration methods, both temperature and polynomial path thermodynamic integration[19] and Widom particle insertion [20]. In this work the focus have mainly been on the thermodynamic integration methods, with particular focus on the polynomial path thermodynamic integration. This due to the relatively ease one could implement this method into the MD simulation software of Lyubartsev and Laaksonen [21].

Tuckerman [14, pp. 315] states that for a system in state $\mathcal{A}$ transforming into state $\mathcal{B}$ with potential energy functions $U_{\mathcal{A}}(\mathbf{r}_1,\ldots,\mathbf{r}_N)$ and $U_{\mathcal{B}}(\mathbf{r}_1,\ldots,\mathbf{r}_N)$, respectively, we can define

$$U(\lambda,\mathbf{r}_1,\ldots,\mathbf{r}_N) = f_1(\lambda)U_{\mathcal{A}}(\mathbf{r}_1,\ldots,\mathbf{r}_N) + f_0(\lambda)U_{\mathcal{B}}(\mathbf{r}_1,\ldots,\mathbf{r}_N), \tag{3.36}$$

where $f_1(\lambda)$ and $f_0(\lambda)$ are switching functions defined such that

$$\begin{aligned} f_1(0) &= f_0(1) = 0 \\ f_1(1) &= f_0(0) = 1. \end{aligned} \tag{3.37}$$

The easiest case where this holds true is for $f_0(\lambda) = 1-\lambda$ and $f_1(\lambda) = \lambda$, where $\lambda \in [0,1]$. In effect this will switch the state from $\mathcal{A}$ to $\mathcal{B}$. In the polynomial path thermodynamic integration formalism from Mezei [19] the choice of λ is somewhat different as seen in Equation 3.38.

$$f_1(\lambda) = \lambda^k \text{ and } f_0(\lambda) = (1-\lambda)^k \tag{3.38}$$

The free energy difference can be found by integrating over λ

$$\Delta A = A_1 - A_0 = \int_0^1 \left\langle \frac{\partial U(\lambda,\mathbf{r}_1,\ldots,\mathbf{r}_N)}{\partial \lambda} \right\rangle_\lambda d\lambda. \tag{3.39}$$

Inserting Equation 3.38 into Equation 3.39 and calculating the partial derivative results in

$$\Delta A = \int_0^1 k[(1-\lambda)^{k-1}\langle U_{\mathcal{A}}\rangle_\lambda + \lambda^{k-1}\langle U_{\mathcal{B}}\rangle_\lambda]\, d\lambda. \tag{3.40}$$

In Mezei [19]'s work the idea is to integrate over a polynomial path evaluated using Gaussian quadratures.

3.2 Force fields

The governing equations of MD are Newton's laws and known to be conservative, thus particles will continue along the direction of their velocity vector unless they interact with other particles or fields. The interaction parameters for particles are given by force fields, describing the interactions in form of equations and force constants, the latter which determines the strength of the interaction. The force fields are a requirement in MD. Thus a major part of running molecular dynamics simulations is to obtain, by finding or creating, a suitable force field for the application in hand.

The task of doing so may seem trivial at first, but is one of utmost importance and harder than it might look. More time is spent on choosing the correct force field, and to verify that the force field is suitable, than for instance the construction of the simulation systems. Water, which only contains three atoms, is a small molecule. In spite of its size, it is surprisingly difficult to simulate. There exists a multitude of different models, yet none of them are capable to correctly display all the properties of water. Some models are good at replicating the diffusional properties in liquid state, others are tailored to obtain the correct crystal structure as ice. However, no model – at this time – is capable of replicating the true behavior of water. With this in mind is should be clear that choosing force fields is crucial for quality simulations and and important aspect of molecular simulations.

Rather than forces, the force field give the means to calculate the potential energy (U), when the positions of all the particles in the system is known. The forces are then obtained by taking the negative gradient of the potential energy (see subsection 3.1.2). A general expression for the potential energy is

$$U = U_{el} + U_{vdW} + U_{bond} + U_{angle} + U_{dihedral}, \tag{3.41}$$

where the contributions are from electrostatic interactions (U_{el}), and van der Waals interactions (U_{vdW}), bond stretching (U_{bond}), angle bending (U_{angle}) and twisting of dihedral angles ($U_{dihedral}$), respectively. Further terms could also be included, such as cross-interactions when both stretching a bond and bending an angle.

3.2.1 Bonded interactions

The different contributions in Eq. (3.41) are often split into two groups. Non-bonded and bonded interactions, where U_{bond}, U_{angle} and $U_{dihedral}$ are bonded interactions. Bonded interactions are usually[1] intra-molecular interactions, while non-bonded interactions can be both intra- and inter-molecular interactions.

Bonds

Chemical bonds between atoms are often modeled as harmonic bonds, where the two bonded atoms are connected by a virtual spring. This is the well-known ball-and-spring model, and it uses Hooke's law to describe the potential energy;

---

[1] There are special circumstances, or cases, where one could use for instance an harmonic pseudo-bond to ensure that a molecule stays within a certain distance from a surface, molecule, *et cetera*; making the interaction inter-molecular.

$$U_{bond}(r) = \frac{1}{2}k_b(r_{eq} - r)^2, \tag{3.42}$$

where k_b is the bond force constant, r is the length of the bond and r_{eq} is the equilibrium bond length. Another common potential for bonds is the well known Morse potential:

$$U_{bond}(r) = D_e(1 - exp(\alpha[r_{eq} - r]))^2, \tag{3.43}$$

where D_e is the well depth and α is the width of the well. Unlike the harmonic potential, Morse potential can model bond dissociation, as the potential energy approaches the dissociation energy[2] when the bond stretches far enough. This is in contrast to the harmonic potential which, by nature, has no upper limit, see Figure 3.2.

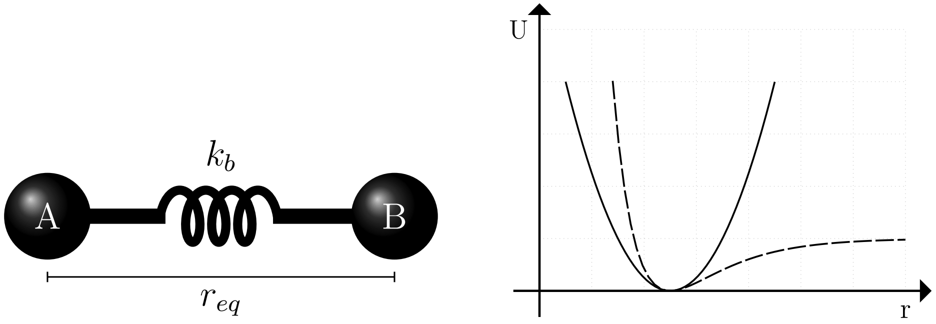

Figure 3.2: Left: Ball and spring model for bond between atom A and B. The equilibrium bond length, r_{eq}, is measured from center to center, k_b is the force constant for the spring (see Eq. (3.42)).
Right: Comparison of a harmonic potential for bond stretching (solid) and a Morse potential (dashed). The units are arbitrary, but both have the minimum at 2.5 on the horizontal axis. Note how the potential energy from the Morse potential approaches a limit as the bond is being stretched.

Angles

Angles are usually modeled using a harmonic style potential, analog to the bonds, but the dependent variable, θ, is now the angle between atoms A–B–C,

$$U_{angle}(\theta) = \frac{1}{2}k_f(\theta_{eq} - \theta)^2, \tag{3.44}$$

where θ_{eq} is the equilibrium angle and k_f is the angle force constant.

Dihedral angles

Dihedral angles are usually modeled in a slightly more complex manner, utilizing Fourier series:

---

[2] This is somewhat simplified in the text. The dissociation energy obtained from the Morse potential is in fact slightly larger than the true value, due to the zero-point-energy stemming from the bond vibrations (see [22, p. 515]).

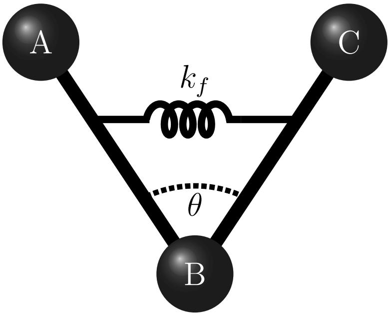

Figure 3.3: Ball and stick representation of the angle between atoms A–B–C. Modeled with a harmonic potential where k_f is the force constant and θ is the angle.

$$U_{dihedral}(\phi) = \frac{V_1}{2}\Big[1+\cos(\phi)\Big] + \frac{V_2}{2}\Big[1-\cos(2\phi)\Big] + \frac{V_3}{2}\Big[1+\cos(3\phi)\Big], \tag{3.45}$$

where ϕ is the dihedral angle between atoms A, B, C and D. $V_1 \ldots V_3$ are the force constants used to describe these somewhat more complex potentials. In Figure 3.4 one can see how ϕ is the angle between the two planes, or the twisting motion around the bond from atom B to atom C. For a molecule to have a dihedral angle, a minimum of four atoms has to be attached in sequence.

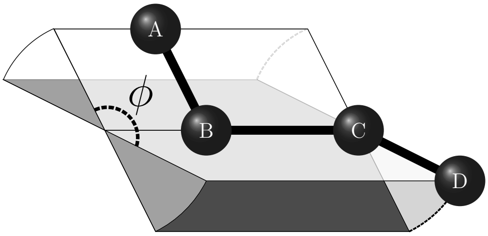

Figure 3.4: Illustration of a dihedral angle between atoms A, B, C and D. The dihedral angle, ϕ, is the angle between the two planes stretched by ABC and BCD, respectively.

3.2.2 Non-bonded interactions

In addition to the bonded interactions there is also non-bonded interactions. These are interactions that can be both intra- and inter-molecular. The non-bonded interactions can be classified in different manners. We can talk about short-range and long-range interactions or van der Waals (vdW) interactions and electrostatic interactions.

van der Waals interactions

The van der Waals interactions, or the short-range interactions, consists of three[3] parts: the Keesom interaction, the Debye interaction and London dispersal forces. Each of these corresponds to a different electrostatic interaction:

Keesom Permanent dipole – permanent dipole interaction.

Debye Permanent dipole – induced dipole interaction.

London Induced dipole – induced dipole interaction.

In sum, we know from statistical mechanics that these interactions, which are all attractive potentials, falls off as a function of $1/r^6$, thus classifying them as short-ranged.

Along with the vdW interactions, a fourth term is merged into the short-range potentials in molecular simulations. This fourth term is repulsive in nature and stems from both Paulie's exclusion principle — that no two electrons may occupy the same spin-orbital — and electrostatic repulsion. Note that the potential for Paulie's exclusion principle is exponential in form.

To model the short-range interactions the Lennard-Jones 12-6 potential is by far the most used and popular potential (see Eq. (3.46)). The Lennard-Jones potential consist of an attractive part, falling off as $1/r^6$, stemming from the vdW interactions, and a repulsive part, falling off as $1/r^{12}$ describing the repulsive part of the potential:

$$U_{ij}(\mathbf{r}) = 4\varepsilon_{ij}\left[\left(\frac{\sigma_{ij}}{|\mathbf{r}_{ij}|}\right)^{12} - \left(\frac{\sigma_{ij}}{|\mathbf{r}_{ij}|}\right)^{6}\right]\delta_{ij}, \tag{3.46}$$

where indices i and j enumerates two different atoms, ε_{ij} is the well-depth of the potential, σ_{ij} is the van der Waals radius and δ_{ij} is a scaling factor. The scaling factor is used in some force field to soften intra-molecular interactions between atoms separated by three bonds (1–4 interactions) and in some cases 1–5 interactions and beyond. $\delta_{ij} \in [0,1]$, as an example the Optimized Potentials for Liquid Simulations (OPLS) by Jorgensen et al. [23] uses a factor of 0.5 for 1–4 interactions and 1.0 for 1–5 interactions and beyond. For atoms separated by less than three bonds the scaling factor is 0.0, or one simply neglects to calculate the interaction, as they are embedded in the bond and angle contributions. It is also prudent to point out that the 12-exponent in the Lennard-Jones potential does not have a true physical meaning. Rather, it was chosen for computational efficiency as it is easy to square the 6-exponent contribution. As mentioned above, the repulsive contribution is exponential in form.

While the Lennard-Jones 12-6 potential is the most popular, the Buckingham potential is also widely used. Similarly to the Lennard-Jones potential, the attractive part falls off as $1/r^6$. The advantage of the Buckingham potential is that the repulsive part is represented by a exponential form. While it is an advantage when thinking of replicating the physical form of the interaction, it is computationally far more expensive.

---

[3] Some people, like Atkins and Paula [22, see p. 696], include the repulsion as a fourth term in the van der Waals forces. Yet others reserve the van der Waals forces for attractive interactions only.

$$U(\mathbf{r}) = A \times exp\left(-B|\mathbf{r}|\right) - \frac{C}{|\mathbf{r}|^6}, \tag{3.47}$$

where A, B and C are constants that determine the strength and shape of the interaction. In some formulations of the Buckingham potential the constant B is given as $B = 1/\rho$ and has units Å. These constants are dependent on which two atoms, or atom types, that interact. See Figure 3.5 for a comparison of the Buckingham potential and the Lennard-Jones 12-6 potential. Another potential draw-back with the Buckingham potential is the infinite attractive well when two atoms are closer than a critical distance (see Figure 3.5). While normally not an issue it can be a cause for some difficulties when initializing a system, or when using some potentials which have a very limited repulsion.

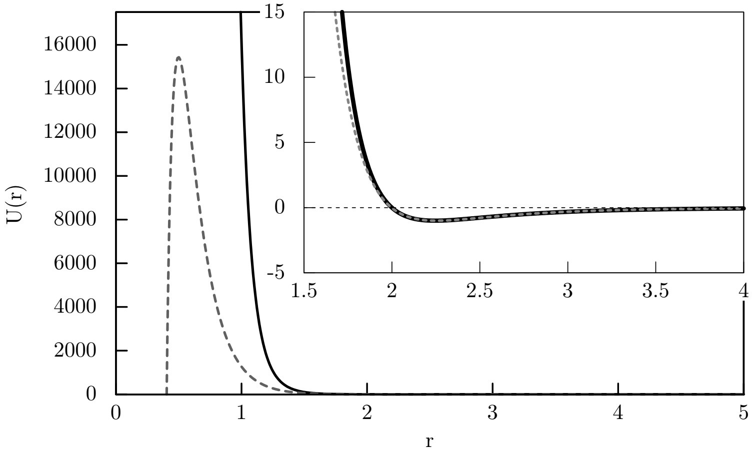

Figure 3.5: Lennard-Jones 12-6 potential (black) and Buckingham potential (dashed gray) in arbitrary units. In this case the Buckingham potential was fitted to reproduce the Lennard-Jones potential. Thus the potentials more or less agree, but the repulsive part differs, with the Buckingham potential being less steep. Also note how the Buckingham potential has a maximum at r=∼0.75. If two particles get closer than this they fall into an infinite attractive potential well.

Electrostatic interactions

Atoms, unless they are ionized, have zero net charge; the same is valid for molecules. However, in a molecule such as water we still observe a dipole moment. To replicate the observed dipole moment in water partial atomic charges are introduced on each atom. That is, permanent point charges are assigned to each atom within a molecule, such that observed dipole – or higher multipole – moments can be reproduced under the constraint that the sum of partial charges within the molecule is zero. The implication of this is that electrostatic interactions are reduced to simple point charge — point charge interactions which easily can be calculated using Coulomb's law (Eq. (3.48)):

$$U_{Coulomb}(\mathbf{r}) = \frac{1}{4\pi\varepsilon_0\varepsilon_r} \times \frac{Q_i Q_j}{|\mathbf{r}|}, \tag{3.48}$$

where ε_0 is the permittivity of vacuum, ε_r is the relative permittivity, Q_i and Q_j is the partial charge of atoms i and j and $\mathbf{r}$ is the vector between those atoms.

The disadvantage with the use of fixed partial atomic charges is that it leaves the model molecule unable to be polarized, by for instance an external electric field, or nearby molecules, atoms or charged surfaces. Some models allow for polarization of the individual atoms. This may increase the qualitative predictions of the simulations but comes at a significant computational cost.

While it is possible to calculate an approximate potential energy arising from electrostatics utilizing Coulomb's law, for large and periodic systems this is computationally very expensive. As electrostatic interactions are long-ranged, they are slow to fall off and is one of the more expensive calculations. Thus, Coulomb's law is often used for the electrostatic interaction within a short range, with a given cut-off radius. Ewald summation methods, or similar methods, which have some addition benefits, are often utilized beyond the cut-off radius (see subsection 3.1.5). This allows for faster electrostatic calculations without introducing artificial artifacts from cutting the tail of the long-ranged interaction.

Chapter 4: Simulation constituents and details

Molecular dynamics is nothing new. One of the first, if not the first paper detailing molecular dynamics simulations is from 1959 by Alder and Wainwright [13]. Alder and Wainwright also wrote a letter to the editor in *The Journal of Chemical Physics* in 1957 where they described how they had used a computer to exactly solve the classical equations of motion for a system consisting of several hundred particles [24]. In the early days they relied on hard sphere, and square well potentials. With time, and computational advances, the potentials have become more complex as well. The advent of more not only more complex, but also a wider selection of, force fields has made the task of selecting the appropriate one for the system in hand a much harder one than in the early days of molecular simulations.

Beyond the rather trivial part of actually running the simulations there are the more non-trivial actions, such as setting up the simulation systems and creating and running post-processing analyzes. This chapter is intended to shed some light on the models used (see section 4.1) and a short physical description of what is being modeled. In the analyzes section (see section 4.2) some analyses will be given in detail along with the concept and idea behind it. I've opted to do this to illustrate the amount of work hidden in figuring out how to best analyze a system, and creating the analyzes.

4.1 Gas, liquid and solid constituents

The majority of my work consists of simulations of complex systems in the way that they include both fluids and solid surfaces. All constituents in any system has to be described by a model, i.e. have some force field parameters assigned. As a side note; a particle without any force field parameters is a particle without any interaction. Such particles are known as *ghost particles*. While such a particle may seem superfluous there exists a use for them (for instance in particle insertion methods for estimating chemical potentials).

Just as the physical counter-parts to the models have physical properties that differs between them, particularly if they exists in other states, so do the models have different properties in terms of functional form and parameters. Gas and liquids usually have functional forms that are more alike and are often utilizing Lennard-Jones interactions and mixing-rules to estimate cross-interactions. Solids, minerals in particular, seems to be described more in terms of pair-potentials, where parameters are given for each particular interaction (often derived from *ab initio* calculations), rather than relying on the use of mixing rules. This use of pair-potentials make force fields for solids more cumbersome to use, in terms of choosing the correct set of parameters, the system setup and in terms of determining cross-interactions. Thus I've elected to separate the constituents into two subsections, one for gas and liquid constituents and one for solid constituents.

4.1.1 Gas and liquid constituents

For the most part the fluids have been restricted to water with dissolved carbon dioxide or hydrogen sulfide. Depending on the system pressure and temperature the constituents have been in gas or liquid state. In some cases, the temperature and/or pressure conditions have been such that one or more of the constituents have been super-critical. In such cases one may have to pay particular attention to the selection of an appropriate force field.

Carbon dioxide

Carbon dioxide is readily available in nature and the main contributor to man-made global warming. To mitigate the impact of global warming the scientific community is focused on reducing the amount released into the atmosphere. This work deals with the subject through molecular modeling. With molecular simulations there may be several different models for even simple molecules. Due to the limitations of classical models the parameters are fitted to replicate the environment of interest. Simulations of CO_2 as a gas may utilize one model with one set of parameters while simulation where CO_2 exists as a super-critical fluid requires a different set of parameters.

The lack of a uniform, fit-all scenarios model can be troublesome. A models that gives excellent performance in a bulk water system may simply be unable to replicate the behavior when it approaches the surface. Such complexities must always be at the attention of the scientist.

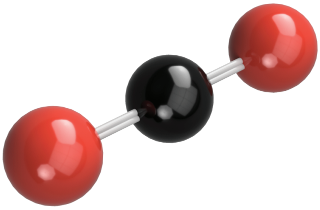

Figure 4.1: Illustration of the carbon dioxide molecule.

While the subject of models may have some complexities as mentioned above, the CO_2 molecule is a rather small molecule consisting of three atoms. Consequently, the models does not contain dihedral angles. As can be seen in Figure 4.1, carbon dioxide is a linear molecule, making the angle approximately 180 degrees. Beyond that, there is a short-range interaction site on each atom, as well as a partial atomic charge. All this, with the bond length and force constants make up the different CO_2-models employed.

In our work we employed different models for CO_2. The EPM2-model from Harris and Yung [25], which is using the Lennard-Jones potential (see Table 4.1 for values), and the Buckingham potential-based model of Tsuzuki et al. [26]. The Buckingham model was primarily used for interactions towards hematite (Fe_2O_3) as quite a few of

Table 4.1: Selected model parameters for CO_2. Bond and angle parameters are specified in the references. (^{a}) Lennard-Jones parameters for the CO_2 EPM2 model by Harris and Yung [25] and Buckingham parameters from the work of Tsuzuki et al. [26]. (^{b}) Lennard-Jones parameters and partial atomic charges from Panhuis et al. [27].

		Lennard-Jones		Buckingham		
Atom	q_c [e]	ε [kJ mol^{-1}]	σ [Å]	A [kJ mol^{-1}]	B [Å]	C [kJ Å^6 mol^{-1}]
C^a	0.6512	0.2339	2.757	909.23	0.3704	1491.6
O^a	−0.3256	0.6694	3.033	1 483 300.00	0.2273	1629.9
C^b	0.6172	0.513 69	3.2618			
O^b	−0.3086	0.810 57	3.0145			

Table 4.2: A summary of some important physical properties of carbon dioxide. Values at 298.15 K and 101.325 kPa (when relevant) Values from "CRC Handbook of chemical properties" [28] if not otherwise specified.

Property	Value	Units
Critical pressure	7.375	MPa
Critical temperature	304.13	K
Density	1.799×10^{-3}	g cm^{-3}
Molecular weight	44.010	g mol^{-1}
Solubility in H_2O	1.5	mol %
Sublimation point	194.686	K
Triple point	216.592	K

the mineral models rely on Buckingham potentials. The model by Tsuzuki et al. [26] is optimized for a supercritical fluid, a vital point worth noticing. Fitting a Lennard-Jones potential to a Buckingham potential can be done, and was one of the solutions chosen in Paper I, but the agreement will never be perfect due to the differences in the repulsive part. It may, however be acceptable within the potential well, see Figure 3.5. After some experimenting, the switch to a Buckingham potential for CO_2 versus $CaCO_3$ was made. In the later work where we estimated free energies of CO_2 in water we utilized the model of Panhuis et al. [27], which was optimized for water-carbon dioxide systems.

Hydrogen sulfide

Hydrogen sulfide has been a problem for the oil and gas industry for a number of years. It is toxic, there are strict limits to how much is allowed in fuel, it is also a very aggressive hydrate former as well as being corrosive. In sum, H_2S is a contaminant and something we would rather not see in process equipment or a pipeline. Nonetheless, H_2S is present in many natural gases, making it unavoidable. If it is present it has to be taken into account when considering flow assurance.

Clathrates are known to be capable of blocking pipelines, creating hazardous situations and process downtime. Hydrogen sulfide, as mentioned above, is a well known

Table 4.3: A summary of some important physical properties of hydrogen sulfide. Values at 298.15 K and 101.325 kPa (when relevant). Values from "CRC Handbook of chemical properties" [28] if not otherwise specified.

Property	Value	Units
Boiling point	213.60	K
Critical pressure	9.00	MPa
Critical temperature	373.1	K
Density	1.393×10^{-3}	$\mathrm{g\,cm^{-3}}$
Melting point	187.65	K
Molecular weight	34.081	$\mathrm{g\,mol^{-1}}$
Solubility in H_2O[29]	1.848×10^{-3}	mol %

and very aggressive hydrate former. Any pipeline streams within the hydrate stability zone containing H_2S has significant chance of experiencing hydrate-related problems.

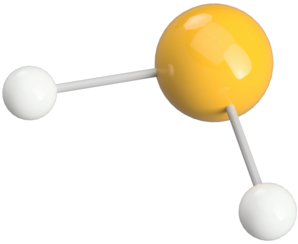

Figure 4.2: Illustration of the hydrogen sulfide molecule.

Hydrogen sulfide as a molecule looks structurally similar to water. It consists of three atoms, two of which is hydrogen atoms bonded to the central sulfur atom (see Figure 4.2). Sulfur, being the next element below oxygen in the periodic table has twice the atomic weight. This give H_2S a molecular weight nearly twice that of water (see Table 4.3). Nonetheless, H_2S is a gas at standard temperature and pressure conditions, where water predominantly exists as a liquid.

In this work H_2S has been modeled using the model from Kristóf and Liszi [30] (see Table 4.4). It is a four-site model, meaning that it contains an additional particle. In this case that particle is a point-charge that lies in the H-S-H plane. The point-charge does not have any short-range interactions. Furthermore, the model only has *one* short-range interaction site, namely the sulfur atom. Just like the point-charge, the hydrogen atoms are only graced with partial atomic charges without any short-range interactions. The model description contains bond lengths and angles, but in this work the H_2S has exclusively been modeled as a rigid molecule. Thus H_2S has only had rotational and translational degrees of freedom. This does leave somethings to be desired, as the effect of bond-vibrations and bending of angles will not be included in the simulations. Yet it is always a matter of consciously deciding what is strictly necessary for achieving the goal. In the simulations where I used H_2S the conclusion was that for the properties of interest the necessity of a flexible model was not present. A rigid model would yield a computational advantage when considering speed. The latter ended up trumping any

Table 4.4: Model parameters for hydrogen sulfide by Kristóf and Liszi [30]. The Lennard-Jones interactions are centered on the sulfur atom, with the hydrogens having only Coulomb interactions. This model also includes a fourth point-charge (PC) in the H-S-H plane.

Charges			Lennard-Jones		Bond and angle		
q_S [e]	q_H [e]	q_{PC} [e]	ε [kJ mol^{-1}]	σ [Å]	H-S [Å]	H-S-H [°]	S-PC [Å]
0.40	0.25	−0.90	2.079	3.73	1.340	92.0	0.1862

Table 4.5: A summary of some important physical properties of water. Values at 298.15 K and 101.325 kPa (when relevant). Values from "CRC Handbook of chemical properties" [28] if not otherwise specified.

Property	Value	Units
Boiling point	373.124	K
Critical pressure	22.06	MPa
Critical temperature	647.10	K
Density	997.0 $\times 10^{-3}$	g cm^{-3}
Molecular weight	18.015	g mol^{-1}
Triple point	273.16	K

potential advantage of a flexible model. It is also prudent to mention that keeping point-charges fixed in plane has previously turned out to be quite troublesome in flexible models.

Water

Water, and modeling water, is an area of great interest by itself. So great that there are books devoted to the subject alone [31]. The deceptively small and simple molecule has a number of different features that has turned out to be of great importance. For instance, water has its greatest density at around 4 °C. Not to mention that ice has a lower density than liquid water. These two properties alone ensures that fresh water lakes and ponds may avoid freezing solid, thus enabling fish to thrive beneath a cover of ice. It is also these complex properties of water that make modeling water troublesome.

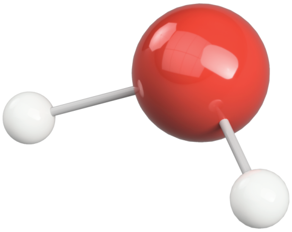

Figure 4.3: Illustration of the water molecule.

Table 4.6: Model parameters for water. Note that the Lennard-Jones, bond and angle parameters are identical for the two first models. The fSPC model is more advanced than the SPC model in terms of allowing flexible bonds and angle, but utilizes the same charges.

	Charges		Lennard-Jones		Bond and angle		
Model	q_O $[e]$	q_H $[e]$	ε [kJ mol^{-1}]	σ [Å]	O-H [Å]	H-O-H [°]	Ref.
SPC	−0.82	0.41	0.6507	3.1656	1.000	109.5	[32]
SPC/E	−0.8476	0.4238					[33]
fSPC	−0.82	0.41					[34]

In the majority of my work I've relied on three water models, namely the simple point charge (SPC) model, extended simple point charge (SPC/E) model and flexible simple point charge (fSPC) model. These are all well-known and renown models. The SPC model is a simple rigid water model. It consists of three point charges with a single short-range interaction site centered on the oxygen atom (see Table 4.6). The O–H bonds are fixed along with the angle, allowing only for translational and rotational degrees of freedom. Later on Berendsen et al. [33] improved on his model and published the extended simple point charge (SPC/E) model. The newer model had some minor changes to the partial atomic charges, but remained otherwise identical to the SPC model. Toukan and Rahman [34] made a flexible model in 1985, where they improved on the SPC model by allowing bonds and angles to be flexible. The fSPC model also contains cross-terms as well as using Morse potential for the bond stretching. In sum, it is considerably more complex than the SPC-model and their paper make for a interesting read.

Many other different water models can be found in the literature, like the TIP4P and TIP5P models. These are four- and five-site models, respectively. The extra sites are additional point charges similarly to the H_2S-model. The TIP5P model was only released as recently as in year 2000 [35]. The authors state that the TIP5P model is capable of reproducing the trend of waters maximum density at 4 °C, which is an improvement over the TIP3P and TIP4P models. More complex models with four and five sites increases the computational demands, which is partly why their development have been held back. Recent advances in computational power makes the computational cost of these models more acceptable. However, the fact that point charges have zero mass makes for some computational difficulties in some code implementations. This did to some extent prevent the use of the TIP4P and TIP5P models in this work.

4.1.2 Solid constituents

The solid constituents in this work has been calcite ($CaCO_3$), hematite (Fe_2O_3) and Linde type A (LTA) zeolite ($\left|\mathrm{M}^{n+}_{12/n}\right|_8[\mathrm{Al}_{12}\mathrm{Si}_{12}\mathrm{O}_{48}]_8$). Calcite and hematite is readily available in nature. $CaCO_3$, for instance, is one of the more abundant minerals. On the other hand, LTA zeolites are synthesized through a rather simple process. Fortunately, when modeling these compounds the origin is not a factor of importance.

Calcite

$CaCO_3$ is a well-known mineral. It can have a wide variety of crystal shapes and colors. One of the more common forms is as limestone formed from marine sediments. Due to the porosity of limestone it may accommodate gas, liquids or even gas hydrates within the rock matrix. If the pores are interconnected and the permeability is sufficiently high, it may even allow for fluids to flow.

In this work the choice to focus on calcite as the reservoir rock came from it being widespread in known oil and gas reservoirs and aquifers. As such it is a likely target for sub-surface carbon sequestration. It is also interesting as it is known to dissolve in low pH environments. Carbon dioxide can react with water and calcite to dissolve the calcite ($CO_2 + CaCO_3 + H_2O \rightleftharpoons Ca^{2+} + 2\,HCO_3^-$) [36]. This reaction could potentially over time dissolve $CaCO_3$ to an extent where the risk of leakage through a fault line is increased.

Conversely, dissolved $CaCO_3$ may precipitate again further from the injection well resulting in reduced porosity and permeability. In theory, a severe reduction in permeability may demand an increased injection pressure, to the point where the increased pressure may fracture the rock matrix. Fracking, or hydraulic fracturing as it is also known, is a technique to modify (increase) the permeability of a reservoir rock through the creation of fractures in the matrix. The technique, when used correctly, can have a significant impact on reservoir flow. However, it is difficult to predict to which extent the rock matrix will fracture, and in which directions the newly formed fractures will go. An unintended fracturing may cause undesirable leakage. It should be noted that this is probably the worst case scenario, and hopefully one that the (injection site) operator would be aware of.

Beside the dissolution and/or precipitation of $CaCO_3$ there is the potential for clathrates to form within the pores of the reservoir or aquifer rock. For hydrate formation to occur the temperature and pressure conditions must be within the hydrate stability zone. Carbon dioxide hydrates are more stable than for instance a methane (CH_4) saturated hydrate. As such, it can form hydrate a conditions where natural gas hydrates would not be formed. A benefit of the increased CO_2 hydrate stability is the potential for exchanging CH_4 guest molecules with CO_2. Injecting CO_2 into a reservoir containing CH_4 hydrate can be used as a method of producing CH_4 through hydrate reformation [37, 38, 39]. CO_2 has a lower chemical potential as a guest molecule than what CH_4 has. The difference in chemical potential give rise to the increased CO_2 hydrate stability and is a driving force for guest–guest exchange.

The calcite mineral has a crystallographic structure belonging to the trigonal crystal system and the $R\bar{3}c$ space group. Its unit cell has sides with lengths a = b = (4.988 ± 0.001) Å and c = (17.061 ± 0.001) Å [40]. The angles are $\alpha = \beta = 90°$ and $\gamma = 120°$ (see Figure 4.4). Stoichiometrically it consists of a calcium ion (Ca^{2+}) and carbonate ion (CO_3^{2-}). By correctly replicating the unit cell one can construct a large block of calcite. For use in the simulations this is exactly what has been done. A crystallographic information file (.cif) with calcite parameters were downloaded from the "American Mineralogist Crystal Struture Database" [41]. This contained the information needed to construct a large crystal which was subsequently cleaved to expose the $10\bar{1}4$ crystallographic plane of interest.

When setting up such a system the total system size in terms of physical size and

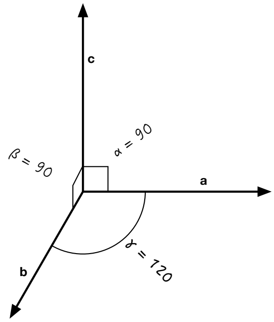

Figure 4.4: Illustration showing the crystallographic axes and angles of the calcite unit cell. See text for parameters.

Table 4.7: Force field parameters for the calcite model used [43]. Note that the charges differ from the original ones (see Cuong et al. [44]).

		Buckingham		
Atom	q_c	A	B	C
	[e]	[kJ mol^{-1}]	[Å]	[kJ Å^6 mol^{-1}]
Ca	1.881	82 942.9	0.455	55 686.7
C	1.482	369 726.0	0.2776	2431.85
O	−1.118	230 235.0	0.2525	1123.6

number of atoms must be kept in mind. Too small and the system may experience unintended self-interactions (through proxy atoms). Too large and the computational demands will make the simulations unfeasible due to time constraints. After the construction of a calcite crystal, force field parameters must be assigned to the atoms (see Table 4.7).

During the simulations carried out within this work, the calcite model was kept fixed. This means that the calcium and carbonate ions did not have any translational or rotational degrees of freedom. It also means that the surface dynamics will be somewhat affected by this as well as the surface structuring of adsorbed molecules. However, the work of Heberling et al. [42] shows that the surface relaxation and restructuring of calcite is relatively small. Thus, the choice of a rigid, fixed, $CaCO_3$ is not unwarranted.

Hematite

Hematite is one of the most thermodynamic stable and abundant iron oxides [45, 46]. It can be found in nature, in the earths crust and in the industries. When iron surfaces oxidizes they are inevitably covered by a layer of iron oxides, or rust. The pipelines traditionally used in the oil and gas industry are made of carbon steel. Due to outside storage and exposure to the elements prior to being installed they may come preequipped with a surface layer of iron oxides.

The crystallographic structure of hematite is a hexagonal unit cell belonging to the trigonal crystal system, with the $R\overline{3}c$ space group [47]. This is the same one as

Table 4.8: Hematite-water parameters from Leeuw and Cooper [48] with charges from *ab initio* calculations Kvamme et al. [49]. The pure Lennard-Jones parameters stems from CLAYFF [50]. Subscript "w" indicates oxygen in water, oxygen in Fe_2O_3 is without subscript.

		Lennard-Jones		Buckingham		
Interaction	q_i $[e]$	ε_{ij} [kJ mol^{-1}]	σ_{ij} [Å]	A [kJ mol^{-1}]	B [Å]	C [kJ Å^6 mol^{-1}]
Fe–Fe	1.31	3.7781×10^{-5}	4.906			
O–O	−0.87333	0.6502	3.1655			
Fe–O_w				42549.82	0.3299	0.0
O–O_w				2196380.31	0.1490	2790.34

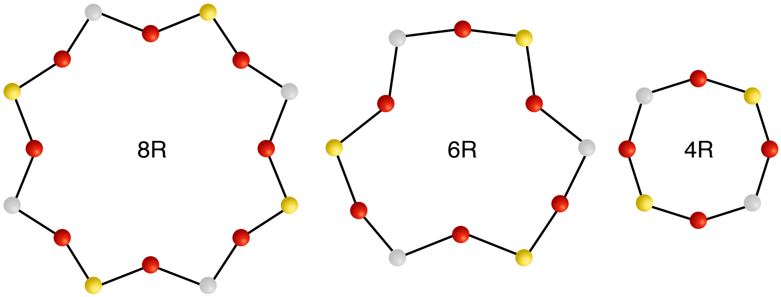

Figure 4.5: Illustration of the 8R (left), 6R (middle) and 4R (right) windows. The numbers 8, 6 and 4 refers to the number of oxygen atoms (red spheres) in the window. The silver and yellow spheres are aluminum and silicon atoms respectively.

for calcite, but for Fe_2O_3 the sides have lengths: a = b = (5.038 ± 0.002) Å and c = (13.772 ± 0.012) Å (see Figure 4.4). The angles remain the same as for calcite. Unlike calcite which was cleaved to expose the $10\bar{1}4$ surface, the 0001 surface of hematite was studied here, based on the arguments presented in Leeuw and Cooper [48] and the abundance of experimental data available for that surface.

The force field employed is given in Table 4.8, and similarly to the $CaCO_3$ systems the Fe_2O_3 atoms where kept fixed during simulation runs.

Linde Type A zeolites

Linde Type A zeolites consists of a framework built by interconnected aluminum, oxygen and silicon atoms. In these structures aluminum and silicon atoms are bonded to four oxygen atoms, making a tetrahedra. Aluminum and silicon are thus known as T-atoms in the realm of zeolites. LTA zeolites belong to the cubic crystal system and have sides a = b = c = (24.555 ± 0.002) Å with angles $\alpha = \beta = \gamma = 90^\circ$ [51].

The aluminum, oxygen and silicon atoms can form different ring structures, denoted 4R, 6R and 8R windows, depending on the number of oxygen atoms in the ring (see Figure 4.5). Combining the rings in the correct structure and you get the LTA framework illustrated in Figure 4.6. Here you see how the 8R-windows allows access into the $alpha$-cavities. The central β-cavities (aka sodalite cavities) can only be accessed through 4R- or 6R-windows. The 4R-windows are too small to allow water molecules to pass. For a framework neutralized by counter-ions, the center of the 6R-windows is one of the favorable counter-ion sites, effectively blocking off the window. In a neutral unit cell there are one counter-ion in each 8R-window and another one in each 6R-window. Additionally, there is a counter-ion inside each α-cavity that positions itself floating slightly above a 4R-window, this is not a fixed position. This last counter-ion can move around inside the cavities.

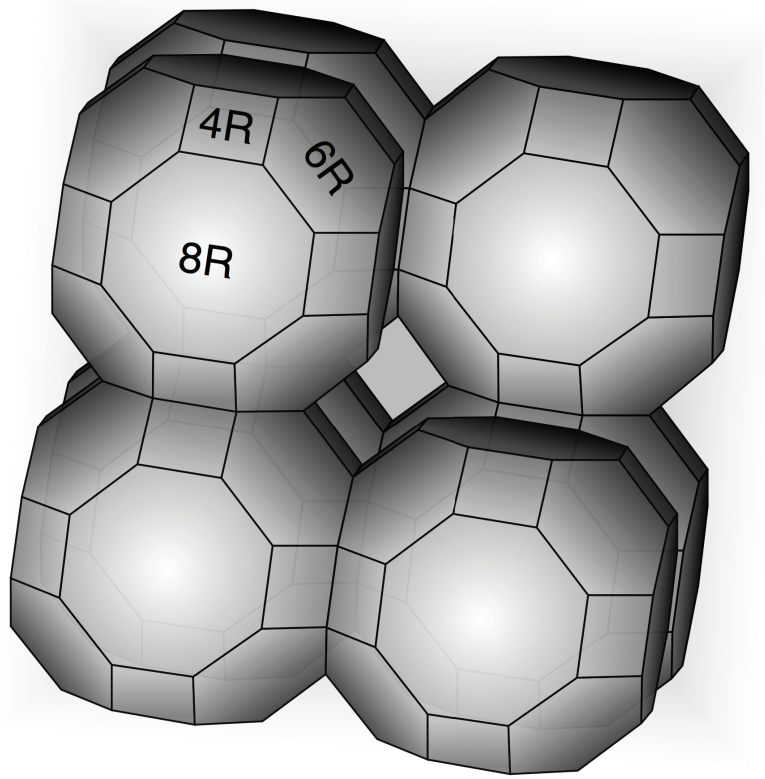

Figure 4.6: Illustration of LTA zeolite framework.

LTA zeolites are synthesized in a relatively easy process. The product from the process is Linde type A zeolites with sodium counter-ions. To obtain LTA-3A zeolite one has to perform an additional process known as ion exchange, where the sodium ions are exchanged with potassium ions. The larger potassium ion reduces the effective opening into the 8R-windows. LTA zeolites are used in a wide range of applications. They are used in laundry detergents, water purifications, water softening, dehydration processes (both industrially and in home appliances), separation, as membranes and as catalysts. The numerous applications has ensured that scientists have devoted lots of interest in the subject, both experimentally and theoretically.

The force field employed on the zeolite simulations stems from the work of Faux et al. [52]. It utilizes a mixture of Buckingham potential and Lennard-Jones potential

Table 4.9: Short-range potentials for framework atoms from [52], potassium parameters from [53]. Water-zeolite potential from [54], and are indicated by subscript "*w*" on water atoms. Water-water interactions modeled using the flexible single point charge model (SPC) [34]. Non-listed interactions are set to 0.

	Buckingham			Lennard-Jones	
Interaction	A [kJ mol^{-1}]	B [Å]	C [kJ mol^{-1} Å^6]	A_{LJ} [kJ mol^{-1} Å^{12}]	B_{LJ} [kJ mol^{-1} Å^6]
Al–O				125 432.97	0.0
Al–O_w				1134.4746	48.2427
Al–H_w				60.3998	7.2364
O–K	96 514.28	0.3620	1019.7540		
O–Na	563 159.47	0.2387	0.0		
O–O	2 196 392.25	0.1490	2050.3135		
O–Si				110 959.935	4824.345
O–O_w				544 676.3125	2260.5549
O–H_w				63 755.3867	522.2751
Si–O_w				1026.9899	56.5404
Si–H_w				53.2599	8.5872
O_w–K	96 514.28	0.3620	1019.7540		
O_w–Na	563 159.47	0.2387	0.0		
O_w–O_w				2 633 780.0	2617.2380

for the short-range interactions. The Lennard-Jones interactions are given as

$$u(r) = \frac{A_{LJ}}{r^{12}} - \frac{B_{LJ}}{r^6}, \tag{4.1}$$

where A_{LJ} and B_{LJ} are the repulsive and attractive terms given in Table 4.9, respectively. Generally one can transform the parameters from the form given here to the more commonly known σ and ε form of the Lennard-Jones potential (see Equation 3.46). To transform back and fourth Equation 4.2 and Equation 4.3 can be used. The calculation of σ and ε is complicated in the case of aluminum-oxygen due to the interaction not having any attractive part (B_{LJ}). This changes the functional form making the two formulations inequivalent, yet in some cases an approximation can be made by curve fitting. Thus approximate values for ε and σ can be obtained if desirable.

$$A_{LJ} = 4\varepsilon\sigma^{12}, \quad B_{LJ} = 4\varepsilon\sigma^6 \tag{4.2}$$

$$\varepsilon = \frac{B_{LJ}^2}{4A_{LJ}}, \quad \sigma = \left(\frac{A}{B}\right)^{1/6} \tag{4.3}$$

The force field by Faux et al. [52] should in theory be capable of replicating a flexible framework. However, in my work the software limited my options to the point where this was unfeasible without significant modifications to the source code. As such, the framework was kept fixed during simulations, only allowing for the counter-ions and water molecules to move.

4.2 Simulation analyzes

Molecular simulation is data generation and gathering. The goal of the simulation is to generate data that hopefully replicates what can be observed in the physical world. On our case that means that we sample the positions, velocities, energies and other properties for atoms, molecules and the system as a whole. These data, generated by the simulation, is the foundation that we through different methods try to analyze and extract information from. It can be as simple as counting or as complex as mapping and evaluating the average potential energy of the system. All to gain a better understanding of the systems and the physics involved. During my research I have had to write several algorithms for analyzing data. Amongst these are algorithms for unfolding the trajectories, calculating mean squared displacements (MSDs), calculating order parameter of water, measuring flux, measuring retention times and for mapping out the potential energy surface with and without short-range interactions. Since this have very much been a part of my day to day work I have opted to write a small text on two of these.

4.2.1 Self-diffusion

There are several methods of estimating self diffusion of molecules in a fluid. Measuring the MSD and using Einstein's relation is one. Using the velocity autocorrelation and integrating the area beneath the curve is another. In my work I used the first method.

To calculate the MSD in a large system is fairly easy. Simply put, to calculate the MSD you take the difference between the position, $\mathbf{r}(t)$, at time t and the position, $\mathbf{r}_0$, at an initial point in time, t_0, and square this difference. If you have more than one particle, which is the case of molecular simulations you average over the number of particles, i.e.:

$$MSD(t) = \left\langle (\mathbf{r}(t) - \mathbf{r}_0)^2 \right\rangle \tag{4.4}$$

However, in most of my systems the molecules would pass through one or more periodic boundaries. This complicates the calculations since the particles suddenly jump from one end of the box to another. If the particles passes through the boundary in the x-direction the x-coordinate will change from for instance 9.99 to -9.99 in a singe time step. Given that the particle continues to travel unabatedly in the same direction the uncorrected MSD will diminish as the particles closes up on its original position.

Due to the complication described above it is necessary to either track the particles as they cross the PBC, or unfold the trajectory prior to running the MSD calculations. Since most simulations consists of a large number of particles, and an even larger number of snapshots in time which the calculations are based on, both of these solutions are quite time consuming. Initially I wrote a tool command language (Tcl) script for the Visual Molecular Dynamics (VMD) application [55] that unfolded the trajectories. However, this was only capable of unfolding the trajectories as long as the particles did not pass through *several* periodic boundaries. Not only that, due to it being a scripting language, and being run inside VMD, it turned out to be very slow.

In the end I had to write a tool to read the trajectory data, keep track of all the particles, and how many boundaries each had passes in all dimensions to be able to calculate the MSDs in this work. In the LTA-systems this was further complicated by the need to exclude the non-mobile water molecules within the β-cavities. This was necessary for having comparable results to that of Faux [56].

4.2.2 Electrostatic potential energy maps

In the zeolite systems I ran into an issue which I assumed was due to electrostatic potential energy gradients within the simulation system. This was something that had to be confirmed, both to bring the issue to the attention of other researchers wishing to go down a similar path, and to figure out a solution to the problem.

While the hypothesis was clear there were no good tools for visualizing the electrostatic potential energy surface. In theory it is quite simple, move a test particle with a known charge on a grid and record the calculated energy at each point. However, once again the PBC complicates the situation. Using Coulomb's law to calculate every interaction for all the grid points would have been very slow. Furthermore, that approach would require some sort of cut-off. A too short cut-off distance and the results would be very poor, too long cut-off distance and the computation would become exceedingly slow. A better approach would be to implement a form of Ewald summation methods. Ewald summation is capable to calculate the electrostatic interaction to an arbitrary precision in periodic systems. It is widely used in molecular dynamics. However, Ewald summation is not particularly fast. It is significantly faster (and more precise) than using Coulomb's law, but there are faster options. The smooth particle mesh Ewald summation method Essmann et al. [15] is one of these methods and the one that was implemented. The gist of this implementation is given in Appendix A (9) and all the relevant equations can be found in subsection 3.1.5.

Initially the program was written to run on the central processing unit (CPU) rather than the general purpose graphical processing unit (GPGPU). However, once the utility was completed it turned out to be much to slow. Due to the massive amounts of calculations involved in creating maps with the desired resolution it would have taken way too long. Rewriting the important parts of the algorithm to run on the GPGPU turn out to be fairly easy and a tremendous time saver.

Chapter 5: Introduction to the papers

As mentioned in section 1.1 the focus has been on examining the potential for hydrate formation during transportation and subsurface storage, with emphasis on using zeolites for gas dehydration as hydrate prevention.

Thus, the papers can be divided into three groups. Paper I deals with water and carbon dioxide interactions with calcite and hydrate surface. Paper II and Paper III covers hydrate formation in and during pipeline transport. These two papers were part of a larger project and as such a group effort. They are based on the rather large written report submitted at the end of the project. The third group consists of Paper IV and Paper V which are focused on zeolites.

Paper I: *Molecular dynamics study of calcite, hydrate and the temperature effect on CO2 transport and adsorption stability in geological formations*

Subsurface storage of CO_2 can be of the utmost importance to reduce the rate of global warming and man-made climate change. But is the effects of injecting CO_2 into the formations understood all that well?

In this paper we study the interactions, adsorption and structuring of H_2O and CO_2 on the *in situ* dominant calcite surface. The system is set up with two solid phases, a $CaCO_3$ and a CO_2 hydrate, to glean important information regarding the potential competition for CO_2. The hydrate surfaces were initially coated by a thin water layer separating it from the carbon dioxide phase. Calcite was coated by a much thicker water layer.

During the simulations two different force field approaches were studied. We started with a hybrid Lennard-Jones/Buckingham force field, and later switched to a purely Buckingham based force field. The differences introduced by the two difference force field approaches were analyzed and compared.

Paper II: *Consequences of CO_2 solubility for hydrate formation from carbon dioxide containing water and other impurities*

Transporting CO_2 to injection sites can be accomplished in different manners, depending on injection site. On-shore injection sites can rely on trucks, trains or pipelines, while off-shore sites may utilize large tankers or pipelines. For large volumes over a long period of time pipelines are the superior option, despite the greater initial cost.

Traditionally the industry have used water dew-point calculation for hydrate risk evaluation. In a pipeline transporting CO_2 and impurities to the injection site – in low temperature and high pressure conditions – the risk of hydrate formation may be given by other factors than the dew-point of water. Here we investigate and formulate a strategy for hydrate risk evaluation in these conditions.

The paper deals with the formalities of absolute thermodynamics, estimation of chemical potentials as a basis for evaluating if hydrate formation will occur or not. We have also included H_2S, an aggressive hydrate former, as an impurity in the gas stream. For each of the paths to hydrate formation given in the paper, the thermodynamic equations necessary are given.

The implications of hydrophilic surfaces, such as oxidized pipeline walls, are investigated in terms of the potential for water adsorbing onto the surface earlier than dictated by dew-point calculation estimates.

Paper III: *Water-wetting surfaces as hydrate promoters during transport of carbon dioxide with impurities*

In the same settings as for Paper II the effect of water-wetting surfaces, more specifically hematite (Fe_2O_3), on hydrate formation is examined. Where Paper II concentrated more on the concept and formalism we extend this here and take a closer look at the adsorption of CO_2 and H_2S onto Fe_2O_3.

The focus is on the total chemical potential for adsorbed carbon dioxide and hydrogen sulfide estimated from molecular dynamics simulations. These are compared towards the total chemical potential for adsorbed water and water participating in hydrate cavities. Finally, the preferential orientation of H_2S adsorbed on hematite is studied.

Paper IV: *The impact of electrostatics in bulk Linde type A zeolites*

The focus now shifts towards LTA zeolites and their properties depending on the choice of counter-ions. A flexible water model was introduced in the zeolite and comparisons were made towards previous work by other groups. The paper reports results from calculations of self-diffusivities and water distributions for the flexible water model in both LTA-3A and LTA-4A.

Initial attempts to move towards more realistic interfacial systems are also made. The efforts reveal that interfacial termination and electrostatics are vital for correct modeling.

We then visualize the electrostatic potentials present in the interfacial system and examines the possibility, and effect, of reducing the partial atomic charges.

Paper V: *The effect of interfacial charge distributions and terminations in LTA zeolites*

Progressing from Paper IV the study of LTA zeolites are moved to more complex interfacial systems. Larger interfacial systems consisting of two unit cells in the longitudinal direction, not including the interfacial termination, are set up. The systems get two different terminations, noted as S4R and D4R terminations. Additionally the D4R systems are ran with six different charge distributions in the interface.

Initially the systems are only partially hydrated, containing only 224 water molecules in total, corresponding to half of the experimentally determined usual loading. On the outside of the zeolite there is a large water phase, capable of supplying the zeolite with more than enough water to become fully hydrated.

The effects of termination and interfacial charge distributions on water structuring, densities and rates of loading are examined. Extending on the previous work, the consequences of improperly handling of partial atomic charges are visualized and identified.

Chapter 6: Conclusions

Our study of the calcite surface adsorption and structuring of carbon dioxide and water showed that temperature were of importance, in terms of both interface and adsorption stability. The study also highlights the importance of proper potentials and the need for better experimental data for comparison and fitting purposes.

When considering pipeline transport of carbon dioxide proper hydrate risk evaluation is critical for proactive hydrate prevention. Thus, more complex models than simple dew-point calculations should be considered. The strategy illustrated may be one such viable method. The work in Paper II and Paper III show that water adsorbing onto solid surfaces may be the deciding factor. While it is shown that the chemical potential of the innermost layers, those directly adsorbed to the surface, prevents hydrate formation those layers rapidly approach what is free water. Thus, hydrate has a real possibility of forming on the outskirts of the adsorbed water layers. There the guest molecules will be readily available too, simplifying mass transport, while the adsorbed water and solid surface can allow for effective heat dissipation.

While hydrogen sulfide is an aggressive hydrate former on its own, it is in low concentrations not capable of forming stable hydrate on its own, but rather assists in stabilizing carbon dioxide-hydrate. hydrogen sulfide was found to adsorb strongly onto the hematite surface, but this may still fail to prevent it from forming a mixed hydrate with carbon dioxide.

Since water has shown such a strong affinity for hematite, adsorbing prior to reaching the dew-point drop out concentrations, dehydration of the gas stream may be necessary to prevent hydrate formation. Linde Type A zeolites have been widely used for dehydration purposes. As carbon dioxide is capable of entering the zeolite when using sodium as counter-ions to balance the structure, it was desirable to extent the studies to potassium counter-ions. We show that the larger counter-ions drastically affects the water diffusion. Furthermore, the accessible volume for water is significantly reduced. When modeling interfacial systems proper surface-termination and corresponding charge distribution is key.

We conclusively visualize and demonstrate how interface termination, and perhaps even more importantly charge distribution affect water structuring, rates of loading as well as interfacial and bulk dynamics. Poor choices, such as changing bulk charges to compensate for interfacial imbalance, skews the dynamics of the system.

Chapter 7: Suggestions to future work

The Achilles' heel of molecular simulations are the force fields. Without proper force fields the results may be biased one way or the other. This make the need for often lacking representative experimental data grave. While fitting potential parameter to experimental results may be very fruitful, employing other means such as Car-Parrinello [57] molecular dynamics or Born-Oppenheimer molecular dynamics may be another approach. While these methods are more demanding with regards to computational complexities, they can form a basis for fitting potentials or reference state in lack of experimental information.

Investigation and calculation of chemical potential is tricky at best. For instance, In the polynomial path thermodynamic integration approach the interactions are scaled, in essence, from their real potential to 0. This, when in presence of a surface and competing species will eventually lead to the molecules being desorbed from the surface. Thus, the contributions sampled after desorption is very likely from a different state or phase. Exploring different methods may be necessary to get better estimates for chemical potential. Perhaps particularly so for hydrogen sulfide, which displayed this exact behavior. More advanced methods could perhaps more precisely predict the adsorbed water layer thickness necessary for hydrate formation to become favorable. Such information can further improve our abilities to predict, and prevent, hydrate formation.

The calcite systems, while the work has been advanced later on by others in the group, could benefit from an increase in complexity. While the effect of a flexible crystal, or flexible surface layers may not be of critical importance for simple systems, the inclusion of ionic species (Ca^{2+}, HCO_3^-, H_3O^+, OH^-) can potentially skew the CO_3^{2-} orientation to a greater extent than water. These are ionic species that inevitably will be present in a system with water and dissolved carbon dioxide. It is prudent to recall the effect of strong electrostatic gradients in the interface regions of these systems, or in the case of defects in the crystal structure.

Linde Type A zeolites, while their structure is very well known and understood still presents a significant amount of questions. Not the least when considering the surface. Experimental results, scanning electron microscopy imaging, indicates that the D4R surface termination is the correct termination. However, it does not tell if the aluminum and silicon atoms on the termination are hydroxylated (a not unreasonable assumption). Again I propose that we return to *ab initio* methods for clarification. And while it is being done getting estimates for the partial atomic charges in the interface, although not an exact science, might be a good idea.

Another potentially fruitful approach is to set up systems in which the zeolite is a membrane separating water in a high-pressure reservoir from a low-pressure region. This would allow for measuring the flux of water molecules through the LTA zeolite. Such experimental results are readily available. Thus, they can possibly give indications on which terminations and charge distributions are yielding results closest to the experimental data, and thus give confirmation by proxy.

As the concentration of water in the gas/liquid outside the zeolite is reduced, the chemical potential decreases. Grand canonical molecular dynamics can be an approach to investigate the kinetics of such a system for different levels of chemical potential for water. The concept of having a particle source in the outer fluid phase is intriguing.

Bibliography

[1] U. D. FCCC/CP/1997/7/Add.1. *Kyoto Protocol to the United Nations Framework Convention on Climate Change*. Dec. 10, 1997.

[2] A. L. Kohl and R. Nielsen. *Gas purification*. 5th. Gulf Professional Publishing, Aug. 1997.

[3] T. Stocker et al. "Technical Summary". In: *Climate Change 2013: The Physical Science Basis. Contribution of Working Group I to the Fifth Assessment Report of the Intergovernmental Panel on Climate Change*. Ed. by T. Stocker et al. Cambridge, United Kingdom and New York, NY, USA: Cambridge University Press, 2013. Chap. TS, 33–115. DOI: `10.1017/CBO9781107415324.005`.

[4] S. Norway. *Area of land and fresh water, 1 January 2015*. `http://www.ssb.no/en/natur-og-miljo/statistikker/arealdekke/aar/2015-04-09`. 2015.

[5] J. D. Figueroa et al. "Advances in {CO2} capture technology—The U.S. Department of Energy's Carbon Sequestration Program". In: *International Journal of Greenhouse Gas Control* 2.1 (2008), pp. 9 –20. DOI: `http://dx.doi.org/10.1016/S1750-5836(07)00094-1`.

[6] R. Lal. "Carbon sequestration". In: *Philosophical Transactions of the Royal Society of London B: Biological Sciences* 363.1492 (2008), pp. 815–830. DOI: `10.1098/rstb.2007.2185`.

[7] R. Korbøl and A. Kaddour. "Sleipner vest CO_2 disposal - injection of removed CO_2 into the utsira formation". In: *Energy Conversion and Management* 36.6–9 (1995). Proceedings of the Second International Conference on Carbon Dioxide Removal, pp. 509 –512. DOI: `http://dx.doi.org/10.1016/0196-8904(95)00055-I`.

[8] D. C. M. White et al. "Separation and Capture of CO2 from Large Stationary Sources and Sequestration in Geological Formations—Coalbeds and Deep Saline Aquifers". In: *Journal of the Air & Waste Management Association* 53.6 (2003), pp. 645–715. DOI: `10.1080/10473289.2003.10466206`. eprint: `http://dx.doi.org/10.1080/10473289.2003.10466206`.

[9] M. B. Kermani and A. Morshed. "Carbon dioxide corrosion in oil and gas production-a compendium". English. In: *Corrosion* 59.8 (Aug. 2003), p. 659.

[10] P. Servio and P. Englezos. "Effect of temperature and pressure on the solubility of carbon dioxide in water in the presence of gas hydrate". In: *Fluid Phase Equilibria* 190.1–2 (2001), pp. 127 –134. DOI: `http://dx.doi.org/10.1016/S0378-3812(01)00598-2`.

[11] S. Mokhatab et al. *Handbook of Natural Gas Transmission and Processing*. Burlington, MA, USA: Gulf Publishing Company, 2006, pp. –.

[12] A. Rojey. *Natural Gas: Production, Processing, Transport*. Institut français du pétrole publications. Editions Technip, 1997.

[13] B. J. Alder and T. E. Wainwright. “Studies in Molecular Dynamics. I. General Method”. In: *The Journal of Chemical Physics* 31.2 (1959), pp. 459–466. DOI: `http://dx.doi.org/10.1063/1.1730376`.

[14] M. Tuckerman. *Statistical mechanics: theory and molecular simulation*. Oxford University Press, 2010.

[15] U. Essmann et al. “A smooth particle mesh Ewald method”. In: *J. Chem. Phys.* 103.19 (1995), pp. 8577–8593.

[16] H. C. Andersen. “Molecular dynamics simulations at constant pressure and/or temperature”. In: *The Journal of Chemical Physics* 72.4 (1980), pp. 2384–2393. DOI: `http://dx.doi.org/10.1063/1.439486`.

[17] S. Nosé. “A unified formulation of the constant temperature molecular dynamics methods”. In: *The Journal of Chemical Physics* 81.1 (1984), pp. 511–519. DOI: `http://dx.doi.org/10.1063/1.447334`.

[18] W. G. Hoover. “Canonical dynamics: Equilibrium phase-space distributions”. In: *Phys. Rev. A* 31 (3 Mar. 1985), pp. 1695–1697. DOI: `10.1103/PhysRevA.31.1695`.

[19] M. Mezei. “Polynomial path for the calculation of liquid state free energies from computer simulations tested on liquid water”. In: *J. Comput. Chem.* 13.5 (1992), pp. 651–656. DOI: `10.1002/jcc.540130515`.

[20] B. Widom. “Some Topics in the Theory of Fluids”. In: *The Journal of Chemical Physics* 39.11 (1963), pp. 2808–2812. DOI: `http://dx.doi.org/10.1063/1.1734110`.

[21] A. P. Lyubartsev and A. Laaksonen. “MDynaMix – a scalable portable parallel MD simulation package for arbitrary molecular mixtures”. In: *Comput. Phys. Commun.* 128.3 (2000), pp. 565–589.

[22] P. Atkins and J. de Paula. *Atkins’ Physical Chemistry*. Ed. by O. U. Press. 7th. Great Clarendon Street, Oxford OX2 6DP: Oxford University Press, 2002.

[23] W. L. Jorgensen et al. “Optimized intermolecular potential functions for liquid hydrocarbons”. In: *J. Am. Chem. Soc.* 106.22 (1984), pp. 6638–6646. DOI: `10.1021/ja00334a030`. eprint: `http://pubs.acs.org/doi/pdf/10.1021/ja00334a030`.

[24] B. J. Alder and T. E. Wainwright. “Phase Transition for a Hard Sphere System”. In: *The Journal of Chemical Physics* 27.5 (1957), pp. 1208–1209. DOI: `http://dx.doi.org/10.1063/1.1743957`.

[25] J. G. Harris and K. H. Yung. “Carbon dioxide’s liquid-vapor coexistence curve and critical properties as predicted by a simple molecular model”. In: *The Journal of Physical Chemistry* 99.31 (1995), pp. 12021–12024.

[26] S. Tsuzuki et al. “Molecular dynamics simulation of supercritical carbon dioxide fluid with the model potential from ab initio molecular orbital calculations”. In: *Chemical Physics Letters* 255.4–6 (1996), pp. 347 –349. DOI: `http://dx.doi.org/10.1016/0009-2614(96)00397-1`.

[27] M. I. H. Panhuis et al. “A molecular dynamics study of carbon dioxide in water: diffusion, structure and thermodynamics”. In: *Molecular Physics* 94.6 (1998), pp. 963–972. DOI: `10.1080/002689798167539`. eprint: `http://dx.doi.org/10.1080/002689798167539`.

[28] W. M. Haynes. *, ed., CRC Handbook of Chemistry and Physics*. Boca Raton, FL., 2015-2016.

[29] J. li Lee and A. E. Mather. “Solubility of Hydrogen Sulfide in Water”. In: *Ber. Bunsenges. Phys. Chem.* 81 (1977), pp. 1020–1023.

[30] T. Kristóf and J. Liszi. “Effective Intermolecular Potential for Fluid Hydrogen Sulfide”. In: *J. Phys. Chem. B* 101.28 (1997), pp. 5480–5483. DOI: `10.1021/jp9707495`. eprint: `http://pubs.acs.org/doi/pdf/10.1021/jp9707495`.

[31] A. Ben-Naim. *Molecular Theory of Water and Aqueous Solutions*. World Scientific, 2011.

[32] H. Berendsen et al. “Interaction models for water in relation to protein hydration”. In: *Intermolecular forces* 11.1 (1981), pp. 331–342.

[33] H. Berendsen et al. “The missing term in effective pair potentials”. In: *J. Phys. Chem.* 91.24 (1987), pp. 6269–6271.

[34] K. Toukan and A. Rahman. “Molecular-dynamics study of atomic motions in water”. In: *Phys. Rev. B: Condens. Matter.* 31.5 (1985), pp. 2643–2648.

[35] M. W. Mahoney and W. L. Jorgensen. “A five-site model for liquid water and the reproduction of the density anomaly by rigid, nonpolarizable potential functions”. In: *The Journal of Chemical Physics* 112.20 (2000), pp. 8910–8922. DOI: `http://dx.doi.org/10.1063/1.481505`.

[36] R. A. Feely et al. “Impact of Anthropogenic CO2 on the CaCO3 System in the Oceans”. In: *Science* 305.5682 (2004), pp. 362–366. DOI: `10.1126/science.1097329`. eprint: `http://www.sciencemag.org/content/305/5682/362.full.pdf`.

[37] B Kvamme et al. “Storage of CO 2 in natural gas hydrate reservoirs and the effect of hydrate as an extra sealing in cold aquifers”. In: *International Journal of Greenhouse gas control* 1.2 (2007), pp. 236–246.

[38] B. Kvamme et al. “Hydrate phase transition kinetics from Phase Field Theory with implicit hydrodynamics and heat transport”. In: *International Journal of Greenhouse Gas Control* 29 (2014), pp. 263 –278. DOI: `http://dx.doi.org/10.1016/j.ijggc.2014.08.003`.

[39] K. Baig et al. “Impact of water film thickness on kinetic rate of mixed hydrate formation during injection of CO2 into CH4 hydrate”. In: *AIChE Journal* 61.11 (2015), pp. 3944–3957. DOI: `10.1002/aic.14913`.

[40] S. A. Markgraf and R. J. Reeder. “High-temperature structure refinements of calcite and magnesite”. In: *American Mineralogist* 70.5-6 (1985), pp. 590–600.

[41] R. Downs and M. Hall-Wallace. “The American Mineralogist Crystal Structure Database”. In: *American Mineralogist* 88 (2003), pp. 247–250.

[42] F. Heberling et al. “Structure and reactivity of the calcite–water interface”. In: *Journal of Colloid and Interface Science* 354.2 (2011), pp. 843 –857. DOI: `http://dx.doi.org/10.1016/j.jcis.2010.10.047`.

[43] S. Hwang et al. “Atomistic Simulations of Corrosion Inhibitors Adsorbed on Calcite Surfaces I. Force field Parameters for Calcite”. In: *The Journal of Physical Chemistry B* 105.44 (2001), pp. 10746–10752. DOI: `10.1021/jp010567h`. eprint: `http://dx.doi.org/10.1021/jp010567h`.

[44] P. V. Cuong et al. “Molecular dynamics study of calcite, hydrate and the temperature effect on CO2 transport and adsorption stability in geological formations”. In: *Molecular Physics* 110.11-12 (2012), pp. 1097–1106. DOI: `10.1080/00268976.2012.679629`.

[45] J. L. Junta-Rosso and M. F. H. Jr. “The chemistry of hematite 001 surfaces”. In: *Geochimica et Cosmochimica Acta* 60.2 (1996), pp. 305 –314. DOI: `http://dx.doi.org/10.1016/0016-7037(95)00382-7`.

[46] A. Navrotsky et al. “Size-driven structural and thermodynamic complexity in iron oxides”. In: *Science* 319.5870 (2008), pp. 1635–1638.

[47] R. L. Blake et al. “Refinement of hematite structure”. In: *American Mineralogist* 51.1-2 (1966), p. 123.

[48] N. H. de Leeuw and T. G. Cooper. “Surface simulation studies of the hydration of white rust Fe(OH)2, goethite α-FeO(OH) and hematite α-Fe2O3”. In: *Geochimica et Cosmochimica Acta* 71.7 (2007), pp. 1655 –1673. DOI: `http://dx.doi.org/10.1016/j.gca.2007.01.002`.

[49] *Molecular dynamics studies of water deposition on hematite surfaces*. Vol. 1504. 1. 2012, pp. 780–783. DOI: `http://dx.doi.org/10.1063/1.4771809`.

[50] R. T. Cygan et al. “Molecular Models of Hydroxide, Oxyhydroxide, and Clay Phases and the Development of a General Force Field”. In: *J. Phys. Chem. B* 108.4 (2004), pp. 1255–1266. DOI: `10.1021/jp0363287`. eprint: `http://pubs.acs.org/doi/pdf/10.1021/jp0363287`.

[51] J. J. Pluth and J. V. Smith. “Accurate redetermination of crystal structure of dehydrated zeolite A. Absence of near zero coordination of sodium. Refinement of silicon,aluminum-ordered superstructure”. In: *Journal of the American Chemical Society* 102.14 (1980), pp. 4704–4708. DOI: `10.1021/ja00534a024`. eprint: `http://dx.doi.org/10.1021/ja00534a024`.

[52] D. Faux et al. “Molecular dynamics studies of hydrated and dehydrated Na+-zeolite-4A”. In: *J. Phys. Chem. B* 101.10 (1997), pp. 1762–1768.

[53] R. Jackson and C. Catlow. “Computer simulation studies of zeolite structure”. In: *Mol. Simul.* 1.4 (1988), pp. 207–224.

[54] L Leherte et al. “Effects of long-range interactions in zeolite-like systems: interaction energies and self-diffusion coefficient of water in ferrierite from molecular dynamics simulation”. In: *J. Mol. Catal.* 54.3 (1989), pp. 426–438.

[55] W. Humphrey et al. “VMD: Visual molecular dynamics”. In: *Journal of Molecular Graphics* 14.1 (1996), pp. 33 –38. DOI: `http://dx.doi.org/10.1016/0263-7855(96)00018-5`.

[56] D. A. Faux. “Molecular Dynamics Studies of Hydrated Zeolite 4A”. In: *J. Phys. Chem. B* 103.37 (1999), pp. 7803–7808. DOI: `10.1021/jp9907600`. eprint: `http://pubs.acs.org/doi/pdf/10.1021/jp9907600`.

[57] R. Car and M. Parrinello. “Unified Approach for Molecular Dynamics and Density-Functional Theory”. In: *Phys. Rev. Lett.* 55 (22 Nov. 1985), pp. 2471–2474. DOI: `10.1103/PhysRevLett.55.2471`.

Chapter 8: Scientific results

Appendix A

Smooth particle mesh algorithm

The main part of the utility (Algorithm 1) loads the coordinates of all atoms into a vector of objects of type Atoms. The atom class is a simple class, holding the name of the atom, its index, total number of atoms, x, y and z coordinates and the partial atomic charges.

```
Algorithm: main
Data: xyz-coordinate file with charges, box size, number of k-vectors, spline order,
      $\beta$-parameter
Result: System electrostatic energies and a grid map of the electrostatic energy

/* Initial setup routines                                              */
Load(filename.xyz);
SetupKSpace(kx-dim, ky-dim, kz-dim);
SetupBox(x-dim, y-dim, z-dim);
SetSplineOrder(n);
SetBeta($\beta$);

/* Carry out the actual calculation                                    */
FillArrays(numProcs);
$\tilde{E}_{rec}$ = CalculateEReciprocal();
ComputeOnCuda();

/* Write output and finish                                             */
WriteDXOutFile();
ResetCudaDevice();
```

Algorithm 1: Main function calls in utility

The algorithm takes as input the desired resolution of K-space along with the periodic boundary conditions (dimensions in x, y and z), and the grid resolution for the test particle. Furthermore, the user specifies the spline order and the β-parameter.

Once the necessary input is provided, the utility continues to calculate the values for B, C and Q arrays, according to equations 3.29, 3.30, 3.31, respectively via algorithm 2. After this point it proceeds to calculate the reciprocal contribution to the systems energy, $\tilde{E}_{rec}$.

```
Algorithm: FillArrays
Data: Vector of Atoms, Spline-object, Arrays
Result: Populated B, C and Q-Arrays
for $k_1 = 0 \rightarrow K_1$ do
    for $k_2 = 0 \rightarrow K_2$ do
        for $k_3 = 0 \rightarrow K_3$ do
            B($k_1,k_2,k_3$) = BCalculate();            // eq. (3.29)
            C($k_1,k_2,k_3$) = CCalculate();            // eq. (3.30)
            Q($k_1,k_2,k_3$) = QCalculate();            // eq. (3.31)
        end
    end
end
```

Algorithm 2: Function FillArrays(), populates the arrays used in calculation of the electrostatic energies.

```
Algorithm: CalculateEReciprocal
Data: B, C, Q, K$_1$, K$_2$, K$_3$
Result: $\tilde{E}_{rec}$, $(B \star C) \cdot Q$-array
F$^{-1}(Q)$ = FFT3D(Q);
for $k_1 = 0 \rightarrow K_1$ do
    for $k_2 = 0 \rightarrow K_2$ do
        for $k_3 = 0 \rightarrow K_3$ do
            BCQ$^{-1}(k_1,k_2,k_3)$ = B$(k_1,k_2,k_3) \cdot$ C$(k_1,k_2,k_3) \cdot$ F$^{-1}(Q)(k_1,k_2,k_3)$;
        end
    end
end
BCQ = FFT3D(BCQ$^{-1}$);
for $k_1 = 0 \rightarrow K_1$ do
    for $k_2 = 0 \rightarrow K_2$ do
        for $k_3 = 0 \rightarrow K_3$ do
            $\tilde{E}_{rec}$ += K$_1\cdot$ K$_2\cdot$ K$_3\cdot$ BCQ$(k_1,k_2,k_3) \cdot$ Q$(k_1,k_2,k_3)$;
        end
    end
end
return $0.5 \cdot \tilde{E}_{rec}$;
```

Algorithm 3: Function CalculateEReciprocal() - Does the inverse Fourier transform of Q-array, multiplies B and C arrays with Q^{-1}-array, and then does a forward Fourier transform of the product. The resulting array is stored for further use.

The reciprocal contribution to the systems energy is calculated by the function CalculateEReciprocal, shown in Algorithm 3. This function performs an inverse Fourier transform of the "grid charge array", Q, and returns $\mathrm{F}^{-1}(Q)$. In the CUDA accelerated implementation for generating the electrostatic map, the convolution of B and C-arrays, multiplied with the $\mathrm{F}^{-1}(Q)$-array is needed. This is calculated here and stored for later use. Thus the function loops over K_1, K_2 and K_3, and performs the element-wise multiplication of B, C and $\mathrm{F}^{-1}(Q)$-arrays. A forward Fourier transform is then carried out on the resulting array, returning a new array denoted as BCQ, see algorithm 3.

Now $\tilde{E}_{rec}$ can be calculated by once again looping over K_1, K_2 and K_3, and summing up the product of the BCQ-array with the Q-array and K_1, K_2, K_3. Finally, $\tilde{E}_{rec}$ is multiplied by the prefactor of 0.5 from Eq (3.32) and the reciprocal contribution is returned.

To generate the electrostatic map, a test particle has to be placed at the desired grid points. The resolution for the number of grid points for the test particle, is provided as input by the user. Then the utility generates $xSteps \cdot ySteps \cdot zSteps$ points in space, and subsequently the same number of Q_{test}-arrays (see algorithm 4). For each new grid point, a new set of scaled fractional coordinates were calculated for the test particle. These were then transferred to the GPU memory and a Q_{test}-array was computed based on equation (3.31), containing only the contributions from the test particle. Then, for each Q_{test}-array, i.e. each grid point, $\tilde{E}_{rec}$ is computed on the GPU using equation (3.32).

```
Algorithm: ComputeOnCUDA
Data: BCQ, $xSteps$, $ySteps$, $zSteps$, PBC
Result: Electrostatic potential map
// Transfer BCQ-array to GPU memory
for $X = 0 \rightarrow xSteps$ do
    testParticle.SetX($X * PBC_X/dx$);
    for $Y = 0 \rightarrow ySteps$ do
        testParticle.SetY($Y * PBC_Y/dy$);
        for $Z = 0 \rightarrow zSteps$ do
            testParticle.SetZ($Z * PBC_Z/dz$);
            /* Calculate scaled fractional coordinates for testParticle
               and transfer to GPU memory                             */
            // eq. (3.31), CUDA accelerated
            $Q_{test}$ = QTestCalculate();
            // eq. (3.32), CUDA accelerated
            SPME_Calculate();
            // Sum array from above command, CUDA accelerated
            $\tilde{E}_{Array}[Z + zSteps * (Y + ySteps * X)]$ = Reduce();
        end
    end
end
```

Algorithm 4: Function ComputeOnCUDA() - Generates the electrostatic maps. Implemented on a nVIDIA GPU in the CUDA language.

In the end, one has $xSteps \cdot ySteps \cdot zSteps$ points with calculated energies, depending on the position of the test particle. The CUDA implementation allows for the multiplication of the arrays, as well as the generation of the Q_{test}-arrays to be computed within an acceptable time frame.

Now that the reciprocal contribution to the electrostatic energies are calculated, a similar scheme for the direct contributions is needed. This is calculated according to eq. (3.19), and is straight forward to implement. Again, this was done using CUDA to ensure rapid calculations. The energies for each grid point was stored for later output and processing.

The array containing the energies, both the direct and reciprocal contributions, is eventually stored in a DX formatted file, allowing for visualization in VMD. A utility was written for extracting layers from the .DX-file and plotting of maps by interfacing into gnuplot.